

# ELECTROMAGNETIC ELECTRON AND PROTON CYCLOTRON WAVES IN GEOSPACE: A CASSINI SNAPSHOT

B. T. Tsurutani<sup>a</sup>, J. K. Arballo<sup>a</sup>, X.-Y. Zhou<sup>a</sup>, C. Galvan<sup>a</sup>, and J. K. Chao<sup>b</sup>

<sup>a</sup>*Jet Propulsion Laboratory, California Institute of Technology, 4800 Oak Grove Drive, Pasadena, CA 91109, USA*

<sup>b</sup>*Institute of Space Sciences, National Central University, Chung-li, Taiwan, Republic of China*

## ABSTRACT

The Cassini spacecraft flew past the Earth in a trajectory almost along the Sun-Earth line, giving a unique perspective of low frequency waves in geospace. Geotail was immediately upstream of the bow shock nose, allowing for an accurate assessment of the solar wind conditions driving geospace macroscale processes, the latter of which led to microinstabilities and electromagnetic plasma wave growth. We demonstrate the presence of nonlinear cyclotron waves in the foreshock, magnetosheath and outer magnetosphere. Wave modes previously unidentified have been detected in the north tail lobe during substorms. A predominance of right-hand cyclotron waves with  $f \approx 2.0$  Hz (in the spacecraft frame) are detected in the foreshock. The waves are compressional with  $\Delta \vec{B} / B_0 \sim 0.25$ . It is argued that these waves are propagating in the electron cyclotron (whistler) mode and that the waves are generated by low-energy electrons streaming into the upstream region with parallel kinetic energies of tens of eV. This region appears to be a pure electron foreshock. The magnetosheath waves are the largest amplitude ( $\sim 15$  nT peak-to-peak in a  $\sim 30$  nT field) proton cyclotron waves detected in geospace. The wave amplitudes are largest near the bow shock and decrease to  $\sim 8$  nT peak-to-peak near the magnetopause. No discernible mirror mode structures were detected in the magnetosheath. It is possible that a low abundance of  $\text{He}^{++}$  ions in the solar wind high-speed stream may be the cause of the ion cyclotron wave dominance, as previously predicted by theory. However, other explanations are possible as well.

The outer magnetospheric proton cyclotron waves are of low intensity ( $\sim 4$  nT peak-to-peak), and can cause weak proton pitch angle diffusion and concomitant diffuse proton aurora. Large-scale solar wind ram pressure pulses do not appear to be the cause of the magnetospheric waves. However, small scale fluctuations are possible. Two new low-intensity wave modes are identified in the tail lobes associated with substorm events. One mode is a transverse, elliptically polarized  $\sim 7.5$  s wave and the other is a purely compressional ( $\sim 0.1$  nT amplitude) wave, with a  $\sim 8$  s quasiperiod. The latter mode is propagating obliquely ( $\sim 70^\circ$  to  $84^\circ$ ) to the magnetic field.

## INTRODUCTION

The Cassini spacecraft had a unique trajectory in its flyby past the Earth on 18 August 1999. Cassini had a path through the subsolar point of the Earth's foreshock and magnetosheath and then flew through the magnetosphere and down the north lobe of the magnetotail. Cassini exited the dawnside of the

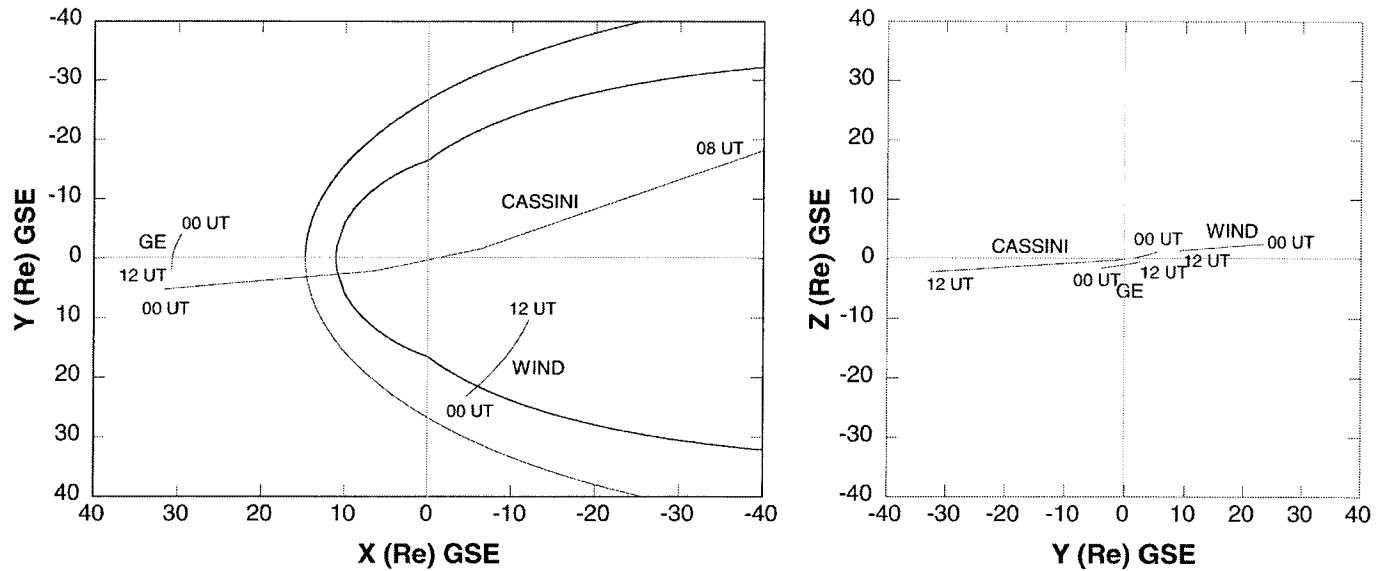


Fig. 1. Trajectories of Cassini, WIND, and GEOTAIL during the Cassini Earth flyby, in GSE coordinates.

magnetotail at  $X \approx -70 R_e$ . This flyby took a total time of  $\sim 10$  hours, thus one can get a unique “snapshot” of low frequency plasma waves in the near-Earth environment. What was particularly striking was that much of this interval was filled with intense, nonlinear electromagnetic plasma waves.

The solar wind interaction with the magnetosphere/magnetotail influences all of geospace, and thus the solar wind is the ultimate source of local plasma instabilities and concomitant wave growth. It was particularly fortunate, during the Cassini flyby, to have the GEOTAIL spacecraft positioned just upstream of the bow shock nose so that it could serve as an upstream monitor. ACE was located farther upstream of the Earth, near the  $L_1$  libration point. Solar wind ram pressure variations lead to magnetosheath/outer magnetosphere/near-Earth magnetotail compressions and rarefactions, and the embedded interplanetary  $B_S$  magnetic fields can lead to magnetic reconnection and substorms (Dungey, 1961). Solar wind velocity and magnetic field directional variations can result in bow shock strength and shock Mach number fluctuations (Kennel *et al.*, 1985). These large scale processes in turn cause microscale processes and plasma instabilities, the topic of this paper.

The Earth’s foreshock is typically dominated by low frequency (10 to 60 s periods) electromagnetic plasma waves occurring in the foreshock (Fairfield, 1969; Hoppe *et al.*, 1981). The waves are associated with energetic ion beams streaming into the upstream medium (Asbridge *et al.*, 1968; Thomsen, 1985, and references therein), and are believed to be generated by an ion-ion instability (Papadopoulos, 1985; Gary, 1991). However, it has been argued that the particle source may be either bow-shock reflected solar wind ions (Bonifazi and Moreno, 1981a,b), escaping magnetospheric ions (Baker *et al.*, 1988; Sibeck *et al.*, 1988), or possibly even energetic electrons (Smith *et al.*, 1976; Goldstein *et al.*, 1985). Foreshock/shock particle energization processes can occur through particle interaction with the waves through either Fermi (Lee, 1982; Forman and Webb, 1985) and/or gradient  $B$  drift shock (Armstrong *et al.*, 1985) acceleration.

The Earth’s magnetosheath is typically dominated by nonoscillatory mirror mode structures (Tsurutani *et al.*, 1982; Anderson *et al.*, 1994), even though the ion cyclotron mode theoretically has higher growth rates (Price *et al.*, 1986). Gary *et al.* (1992), in agreement with the work of Price *et al.* (1986), explained the dominance of mirror mode structures in the magnetosheath as being due to the presence of small amounts of  $\text{He}^{++}$  in the solar wind and magnetosheath (see also Brinca and Tsurutani, 1989). In this

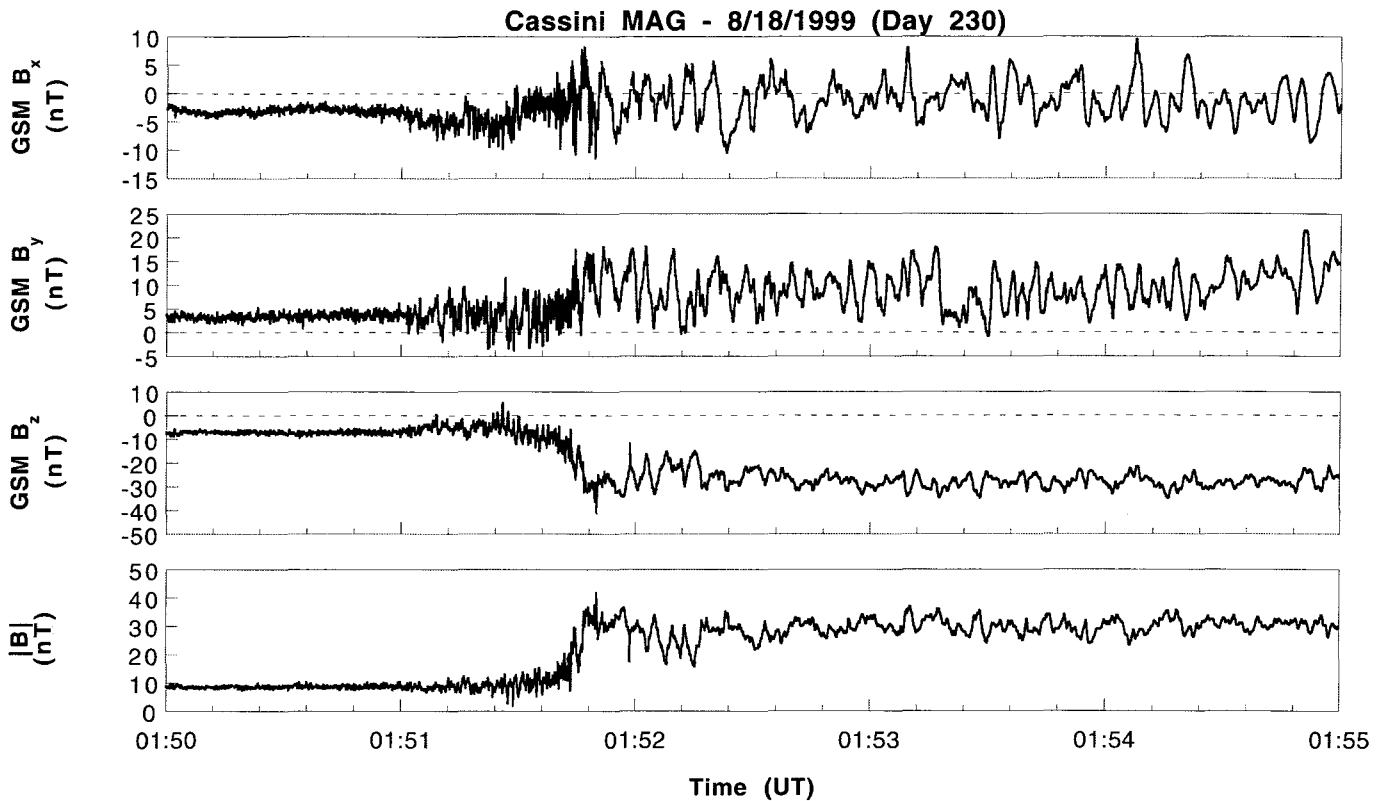


Fig. 2. The Earth's foreshock and magnetosheath waves detected by Cassini. The bow shock is located at  $\sim 01:51:50$  UT.

scenario, the  $\text{He}^{++}$  ions create a stop-band in the proton cyclotron dispersion relationship, effectively reducing the proton cyclotron wave growth rate.

Proton cyclotron waves have previously been detected in the outer magnetosphere during solar wind compression events (Anderson and Hamilton, 1993). The waves are generated by a proton temperature anisotropy ( $T_{\perp}/T_{\parallel} > 1$ ) instability, the latter which results presumably from adiabatic compression of preexisting energetic protons in the outer magnetosphere.

Low frequency electromagnetic waves in the tail (Tsurutani and Smith, 1984) have been ascribed as being due to generation by ion beams streaming away from the tail reconnection  $X$ -line (Cowley *et al.*, 1984; Tsurutani *et al.*, 1985) in the low beta plasmashet boundary layer. This instability has been discussed in detail by Gary *et al.* (1985).

The purpose of this paper is to analyze and characterize the low frequency electromagnetic plasma waves in the four regions of geospace (foreshock, magnetosheath, outer magnetosphere and near-Earth magnetotail lobe), and to determine the solar wind influence (or lack of it) on waves in each region. We will demonstrate that the macroscale properties of the solar wind have significant influence on the wave modes and intensities for these various regions of geospace.

## RESULTS

### Overview

The Cassini encounter trajectory is shown in Figure 1. The left-hand panel shows the trajectory projected into the GSE X-Y plane and the right-hand panel, the trajectory projected into the GSE Y-Z plane. In this

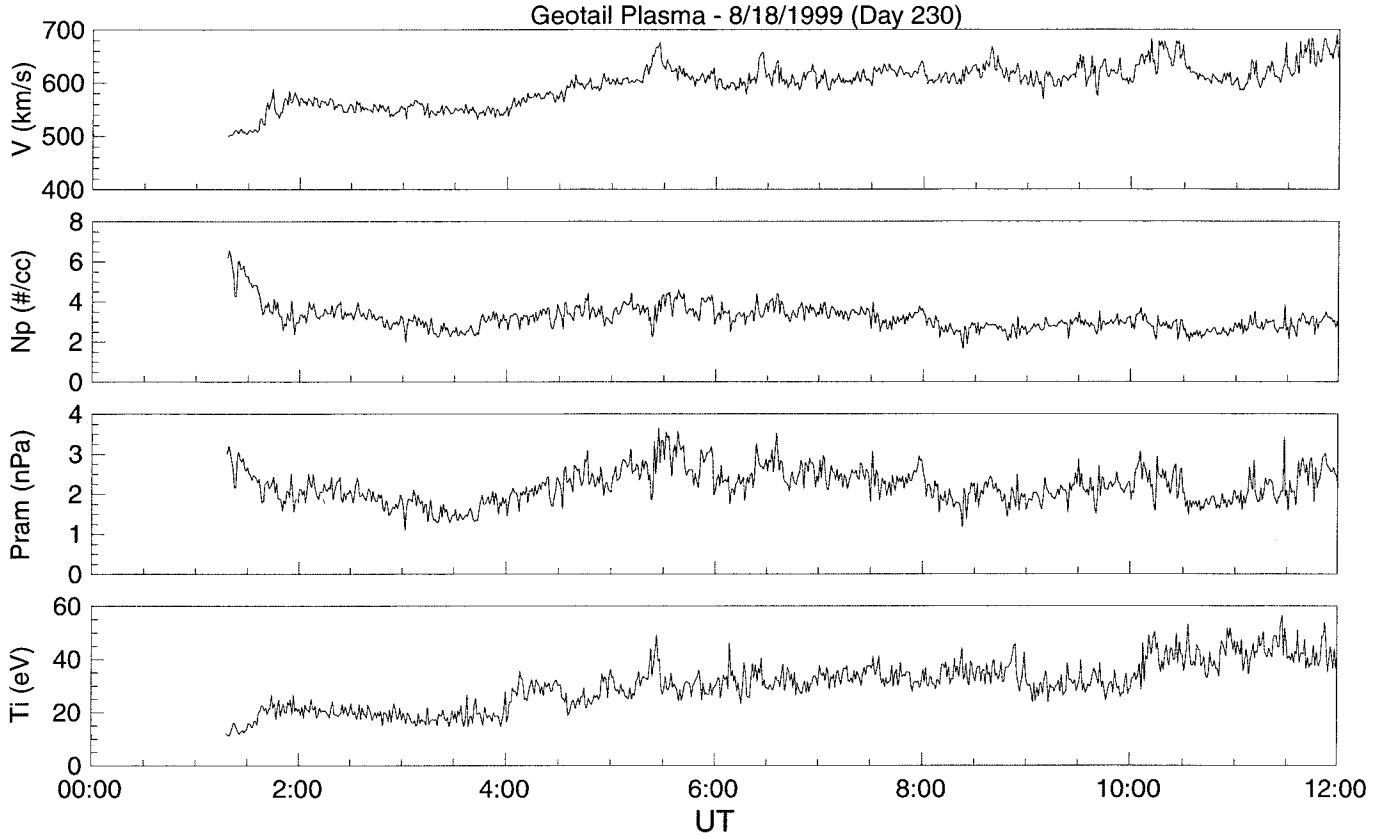


Fig. 3. The upstream solar wind during the time of the Cassini Earth-encounter.

coordinate system  $\hat{x}$  is in the Earth-Sun direction,  $\hat{y}$  is in the plane of the ecliptic in the direction of motion opposite to the Earth's rotation about the Sun, and  $\hat{z}$  forms the right-hand system. Cassini enters the magneto-sheath/magnetosphere essentially along the Sun-Earth line.

The figure also shows the trajectories of two other spacecraft: GEOTAIL (designated by GE), and WIND. GEOTAIL is positioned  $\sim 20 R_e$  upstream of the magnetopause nose, an ideal position to monitor the solar wind conditions and their variations during the encounter. In the figure, WIND starts (at 0000 UT) in the solar wind, then enters the magnetosheath shortly thereafter. Not shown is the ACE spacecraft which is orbiting the  $L_1$  libration point. ACE was at  $(248, -4, 24 R_e)$ .

An overview of the Cassini foreshock and magnetosheath waves is shown in Figure 2. The upstream interplanetary magnetic field (for reference, the bow shock is located at  $\sim 0151:50$  UT) is  $(B_x, B_y, B_z) = -3, +3, -8$  nT, in GSM coordinates. In this system,  $\hat{x}$  is in the direction from the Earth to the Sun,  $\hat{y} = \hat{x} \times \hat{M} / |\hat{x} \times \hat{M}|$ , where  $\hat{M}$  is the south magnetic dipole direction, and  $\hat{z}$  completes the right-hand system. The interplanetary field is a positive sector field (outward from the Sun) with a strongly negative  $B_z$  component. The magnetic field has an orientation  $\sim 70^\circ$  relative to the Sun-Earth line.

Both the  $B_y$  and  $B_z$  components are intensified at and behind the bow shock ( $\sim 0151:50$  UT). The magnitude of the magnetic field increases from  $\sim 8$  nT upstream ( $B_1$ ) to  $\sim 32$  nT downstream ( $B_2$ ). The ratio  $B_2/B_1 \approx 4.0$ , the maximum expected for MHD shocks (Kennel et al., 1985). There is a significant shock "overshoot", where the field reaches  $\sim 47$  nT. "Overshoots" are typically associated with ion deflection at supercritical shocks (Goodrich, 1985).

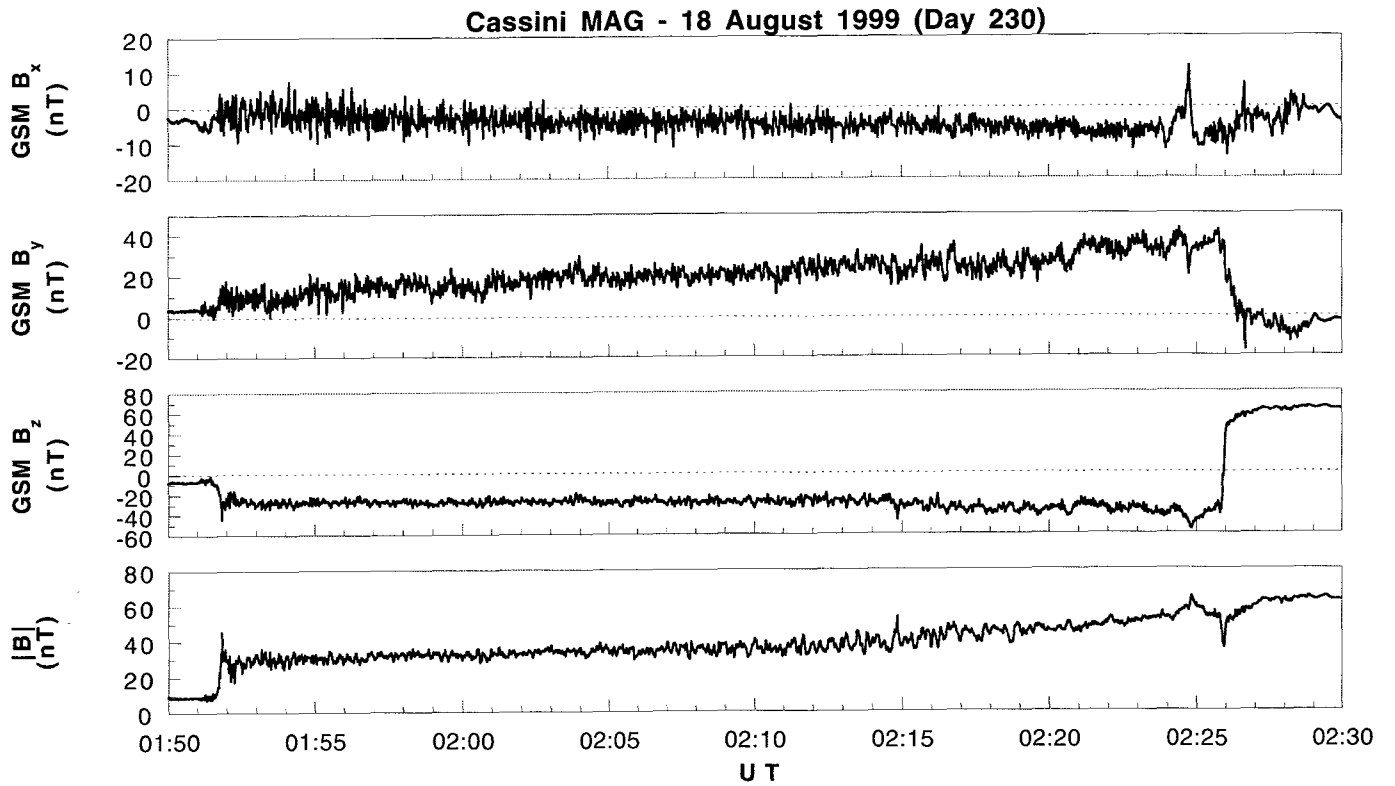


Fig. 4. The magnetosheath magnetic fields and superposed waves.

At 0148 UT at GEOTAIL (Figure 3), the solar wind speed was  $\sim 560 \text{ km s}^{-1}$ , the proton density was  $3 \text{ cm}^{-3}$ , the proton thermal energy was  $\sim 20 \text{ eV}$  and the magnetic field strength was  $8.5 \text{ nT}$ . The Alfvén speed  $(B^2/4\pi\rho)^{1/2}$  was therefore  $\sim 107 \text{ km s}^{-1}$ , the sound speed was  $(\gamma P/\rho)^{1/2} \approx 58 \text{ km s}^{-1}$ , and the magnetosonic speed was  $121 \text{ km s}^{-1}$ . The ion cyclotron, electron cyclotron and electron plasma frequencies were  $1.5 \times 10^{-1}$ ,  $2.3 \times 10^2$ , and  $1.5 \times 10^4 \text{ Hz}$ , respectively. From magnetic coplanarity analyses, the shock normal was determined to be  $\theta_{Bn} = 63^\circ$ , oriented at  $(0.96, -0.29, -0.04)$  in GSE coordinates. The shock magnetosonic Mach number was  $\sim 4.6$ .

Upstream of the shock (Figure 2), foreshock waves had higher frequencies (in the spacecraft frame) than the downstream magnetosheath waves. The foreshock wave amplitudes were largest nearest the shock, and they decreased with increasing upstream distance. This amplitude falloff is consistent with the free energy for wave growth being largest near the shock and decreasing with increasing distance (consistent with a shock-reflected particle beam or magnetospheric particle escape wave generation mechanism).

The post-shock magnetosheath waves were of lower frequency, beginning directly at the shock and continuing into the downstream region to the magnetopause (not shown in this figure). In Figure 2, the waves are noted to be quasiperiodic and are exceptionally large in amplitude. Immediately behind the shock, the waves have  $\sim 15 \text{ nT}$  peak-to-peak amplitudes in a  $\sim 30 \text{ nT}$  field.

Figure 4 shows the full sheath, up to and past the magnetopause (located at  $\sim 0226 \text{ UT}$ ). The magnetic field magnitude slowly increased from the post-shock region ( $\sim 32 \text{ nT}$  as previously stated), to  $\sim 60 \text{ nT}$  just prior to the magnetopause.  $B_y$  increased from  $\sim 10 \text{ nT}$  to  $\sim 30 \text{ nT}$  and  $B_z$  from  $\sim -30 \text{ nT}$  to  $\sim -55 \text{ nT}$  during the same time interval of time. This steady magnetic field magnitude increase with decreasing distance from the magnetopause is due to the Zwan-Wolf (1976) field draping effect, where magnetosheath

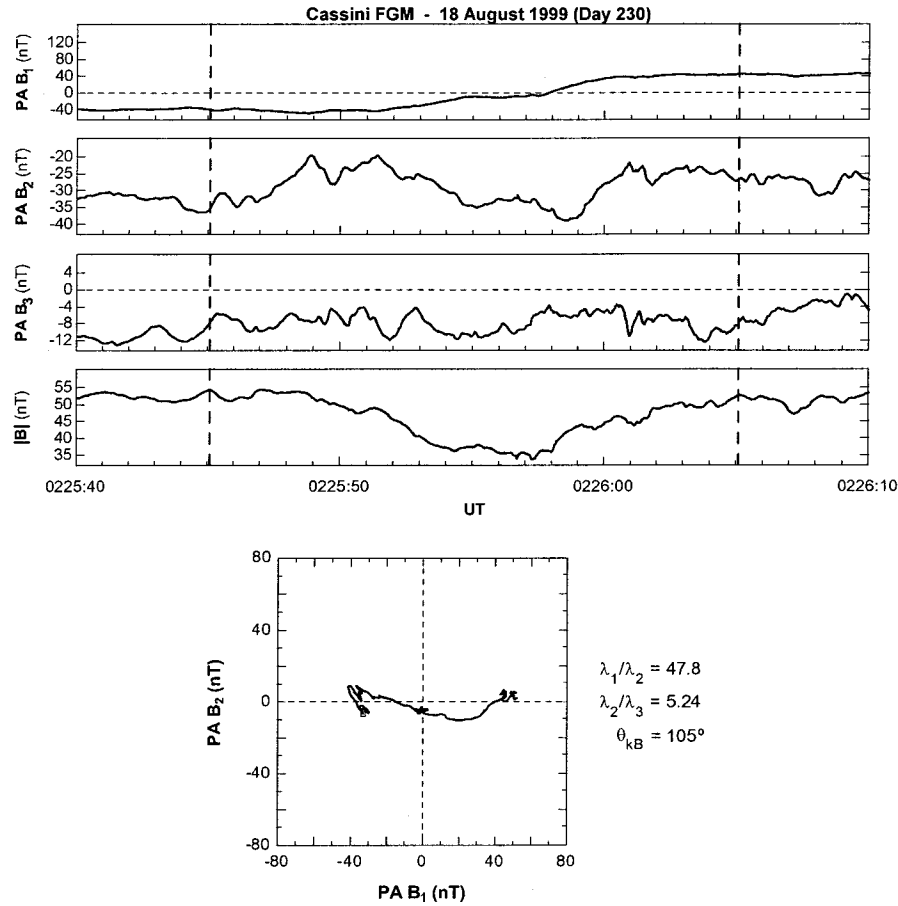


Fig. 5. The magnetic fields at the magnetopause (top panel). The bottom panel is a hodogram of the magnetopause fields.

magnetic fields “drape” around the magnetosphere. As the magnetosheath plasma and fields are convected towards the stagnation point (the magnetopause nose), more and more plasma gets squeezed out the ends of the flux tubes leading to higher magnetic field strengths and lower plasma densities (lower plasma betas) near the magnetopause. This general trend can be noted in the figure.

Although the wave amplitudes were large throughout the magnetosheath, they gradually decreased from the bow shock to the magnetopause. This can be noted in the  $B_x$  component, the component most transverse to the ambient field direction. Another feature of the waves is that they were generally noncompressive. The largest field magnitude variations were present at ~0215 UT with ~6 nT variations in a ~40 nT field. These field decreases were quite small compared to the 50 - 80% variations typical of mirror mode structures (Tsurutani et al., 1982).

### Magnetopause

The minimum variance analysis results of the magnetopause are shown in Figure 5. The analysis was performed on 32 vector-per-second fields, the highest time resolution available for the Cassini magnetometer (Dougherty, et al., 2001). The magnetopause current layer is quite broad, extending from 0225:44 UT to 0226:05 UT. There is a large, steady normal field component ( $B_3$ ) of ~8 nT present. The large normal component indicates that this is a rotational discontinuity (Sonnerup and Ledley, 1974), consistent with the concept that magnetic reconnection is taking place at this boundary (the magnetopause).

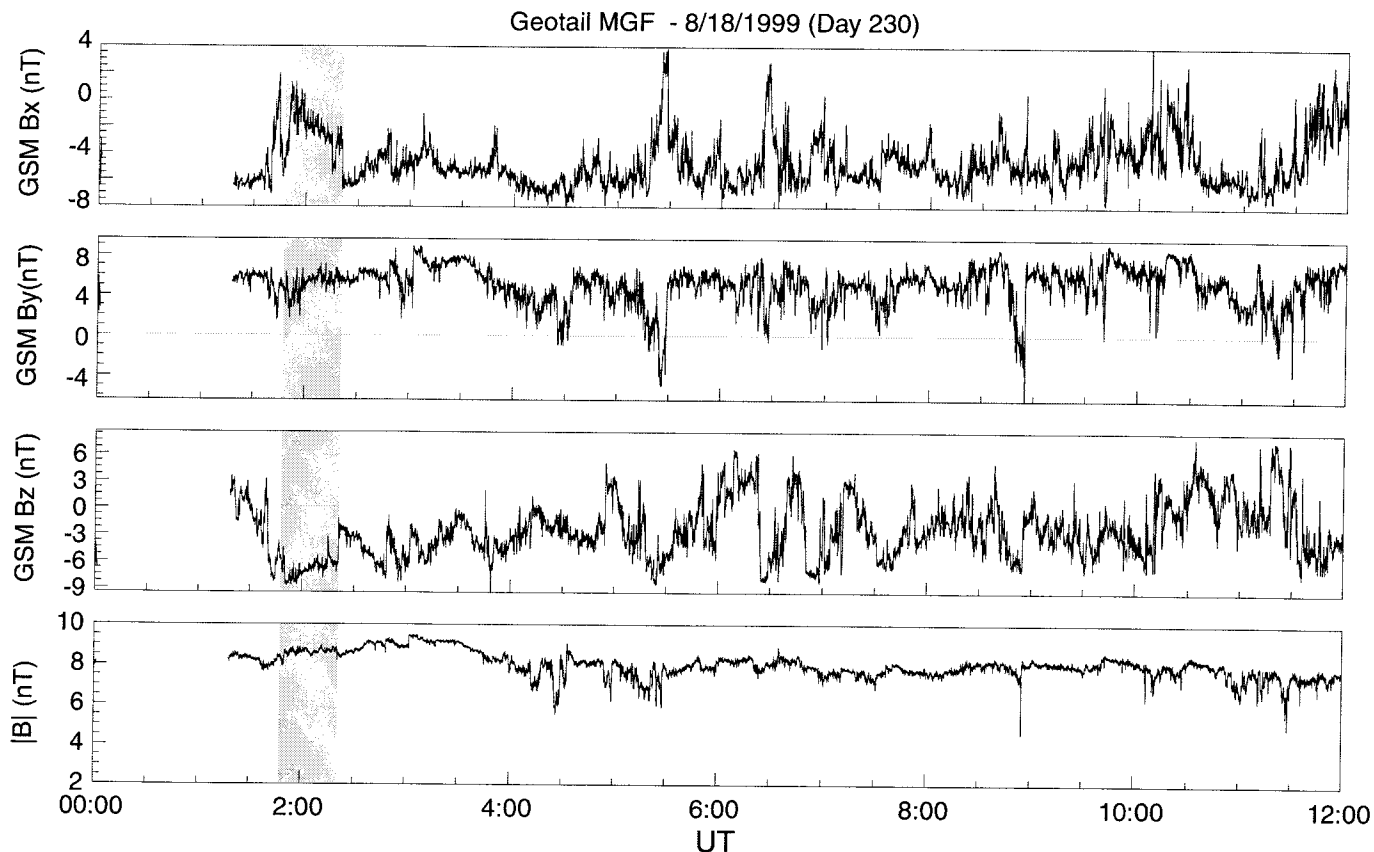


Fig. 6. The interplanetary magnetic field during the time of the Cassini Earth-encounter.

### Solar Wind

Before going into a detailed discussion of the plasma waves, the solar wind plasma and field conditions should be discussed. Both the general state and variations of this interplanetary driver can have significant impact on the magnetosphere interaction, as we will show later.

Figure 3 showed the GEOTAIL solar wind plasma parameters for the Cassini encounter interval (there was a spacecraft tracking gap from 0000 to ~0120 UT but this is not important for this study). The foreshock wave data interval (Figure 2) started at ~0150 UT. The solar wind speed is given in the top panel of the figure. The speed gradually increased from  $\sim 500 \text{ km s}^{-1}$  to  $\sim 680 \text{ km s}^{-1}$  over the  $\sim 10$  hour Cassini interval.

Coincident with this solar velocity increase was a decrease in proton density. The proton density was  $\sim 6.0 \text{ cm}^{-3}$  at 0120 UT and decreased to  $\sim 3.0 \text{ cm}^{-3}$  by 1200 UT. The proton thermal energy increased from  $\sim 10 \text{ eV}$  to  $\sim 45 \text{ eV}$  in the same time interval. The variation of the three parameters indicates that GEOTAIL (and the Earth) were becoming engulfed in a high-speed (coronal hole) stream (Phillips et al., 1994). This general scenario has been verified using the ACE plasma data. A peak velocity of  $\sim 800 \text{ km s}^{-1}$ , minimum plasma density of  $\sim 2.0 \text{ cm}^{-3}$ , and peak proton thermal energy of  $\sim 50 \text{ eV}$  was attained at  $\sim 1200 \text{ UT}$  day 231 (one day later, not shown).

The third panel in Figure 5 gives the solar wind ram pressure. During the Cassini encounter, GEOTAIL was located  $\sim 20 R_e$  upstream of the Earth's magnetopause (assumed to be located at  $x = 10 R_e$ ). The solar wind, with a speed of  $\sim 560 \text{ km s}^{-1}$ , would take  $\sim 4 \text{ min.}$  to convect from GEOTAIL to the magnetopause





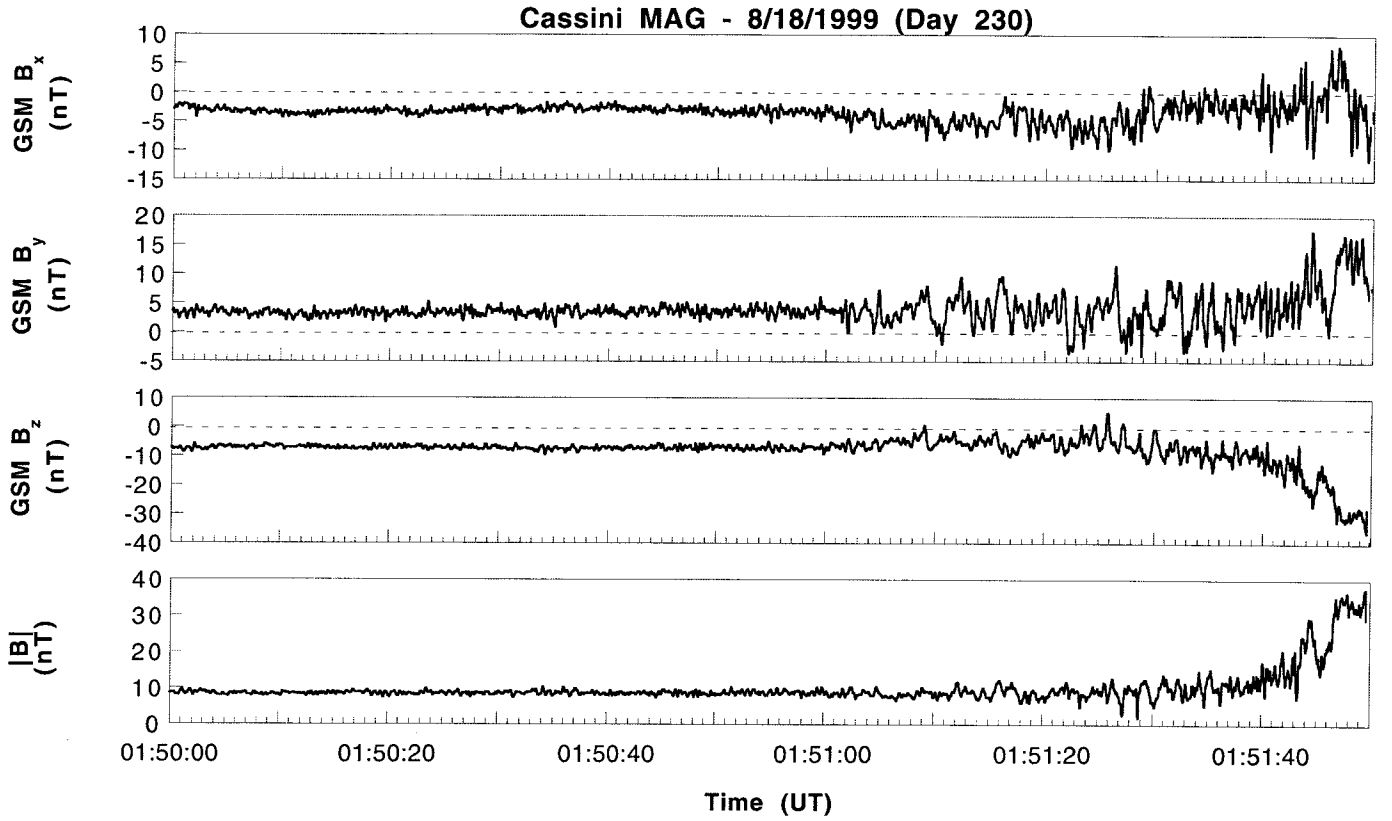


Fig. 8. The Earth's foreshock waves.

magnetic field line tangent to the shock. From measurements just prior to the Cassini bow shock crossing, it was ascertained that the field angle relative to the Sun-Earth line was  $70^\circ$ . This figure assumes that the bow shock is symmetric relative to the x-axis and the magnetic fields are constant in orientation. The distance between the edge of the foreshock and the shock is  $3.3 R_e$ , taken along the Cassini trajectory. This corresponds to  $\sim 22$  min time duration. Thus for steady IMF directions, Cassini should be in the electron foreshock region from  $\sim 0130$  UT to the shock crossing (0151:50 UT).

Figure 8 is an overview plot of the upstream waves, shown in high resolution. The wave amplitudes were largest near the shock,  $\sim 14$  nT peak-to-peak in a  $\sim 35$  nT field with decreasing amplitudes with increasing upstream distance. The waves had  $\sim 7.0$  nT peak-to-peak amplitudes in an  $\sim 8$  nT field at 0151:00 UT. The quasiperiod of the waves was  $\sim 0.8$  s. The high frequency waves have a clear cutoff at  $\sim 0147$  UT. This is caused by the rotation of the magnetic field such that the magnetic field at Cassini is no longer connected to the bow shock.

Figure 9 is an example of one wave cycle from 0151:39.9 to 0151:40.6 UT. The wave peak-to-peak amplitude is  $\sim 14.0$  nT in a  $\sim 15$  nT ambient field. In the hodogram it is noted that the wave was right-hand polarized in the spacecraft frame, nearly circularly polarized ( $\lambda_1/\lambda_2 = 2.0$ ) and planar ( $\lambda_2/\lambda_3 = 2.2$ ). Here the subscripts 1, 2 and 3 correspond to the maximum, intermediate and minimum variance components (Smith and Tsurutani, 1976). The angle of propagation relative to the ambient magnetic field  $\theta_{KB}$  was  $\sim 52^\circ$ .

Figure 10 is a wave cycle far from the shock, from 0151:16.6 to 0151:17.4 UT. The wave peak-to-peak amplitude was  $\sim 8.0$  nT in a  $\sim 10.0$  nT ambient field. The wave was right-hand circularly polarized ( $\lambda_1/\lambda_2$

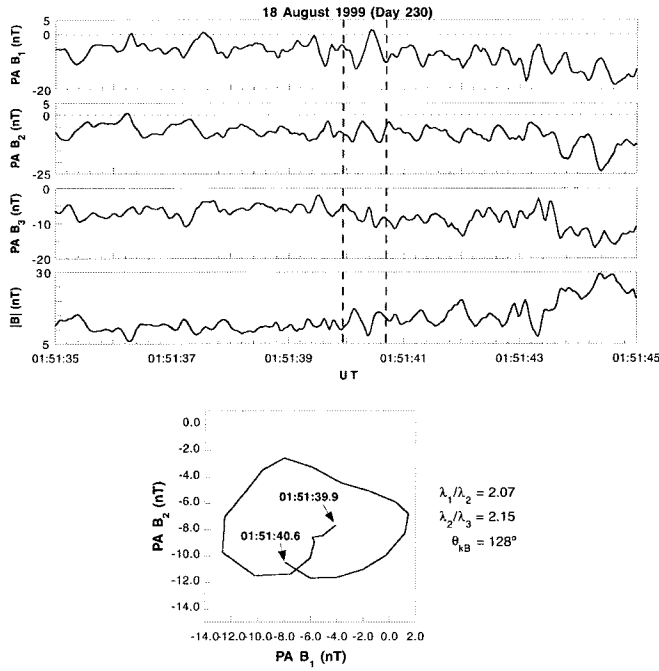


Fig. 9. Hodogram of the wave cycle from 01:51:39.9 to 01:51:40.6 UT.

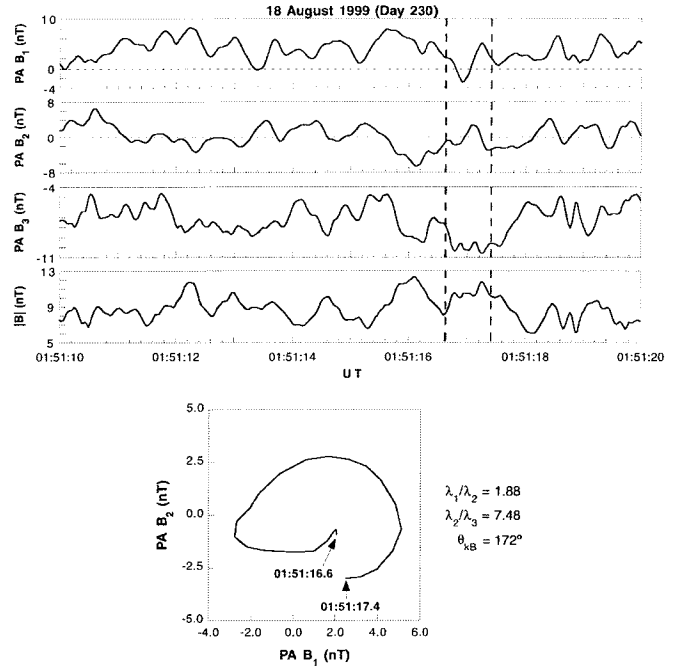


Fig. 10. Hodogram of the wave cycle from 01:51:16.6 to 01:51:17.4 UT.

= 1.9), planar ( $\lambda_2/\lambda_3 = 7.5$ ) and was propagating at an angle of  $\sim 8^\circ$  relative to the magnetic field. There was a  $\sim 2$  nT compressional component associated with the wave.

Table 1 summarizes the wave properties for the region immediately upstream of the shock. The waves were almost all right-hand circularly to elliptically polarized in the spacecraft frame. There were only a few left-hand wave cycles identified. The wave periods range between 0.3 s and 1.3 s in the spacecraft frame, with a median of 0.8 s. 45% of the waves had  $\lambda_1/\lambda_2$  values between 1.0 and 3.0, indicating that the waves were often circularly to elliptically polarized. A normalized (to spherical area) histogram of  $\theta_{kB}$  is given in Figure 11. The waves were propagating at all angles with respect to  $\vec{B}$ , with a slight tendency to propagate along the field line direction.

#### Calculation of Resonant Particle Energies (Generating the Foreshock Waves)

Foreshock plasma waves are generated by energetic protons or electrons that are streaming away from the bowshock/magnetosheath into the upstream region. In this particular case, the solar wind speed was  $\sim 560$  km s $^{-1}$  and the Alfvén speed  $\sim 107$  km s $^{-1}$ . The relevant ion, electron and plasma frequencies were  $1.5 \times 10^{-1}$  Hz,  $2.3 \times 10^2$  Hz and  $1.5 \times 10^4$  Hz, as stated previously.

Several features of the foreshock waves were unusual. First, the vast majority of the waves were right-hand polarized in the spacecraft frame. The waves had magnetic magnitude variations of  $\sim 25\%$ , strong compressional components. Frequencies in the spacecraft frame were  $\sim 1.25$  Hz ( $\sim 0.8$  s periods), considerably higher than  $\sim 10^{-1}$  to  $1.3 \times 10^{-2}$  Hz unusually dominating foreshock waves (Hoppe et al., 1981). Also, foreshock waves are typically left-hand polarized (in the spacecraft frame) rather than right-hand polarized as shown here.

Sentman et al. (1983) have shown that the most likely source of upstream whistler mode waves is  $\sim 20$  eV electrons reflected off of the bow shock. They reported a lack of 1-20 keV electrons during the intervals

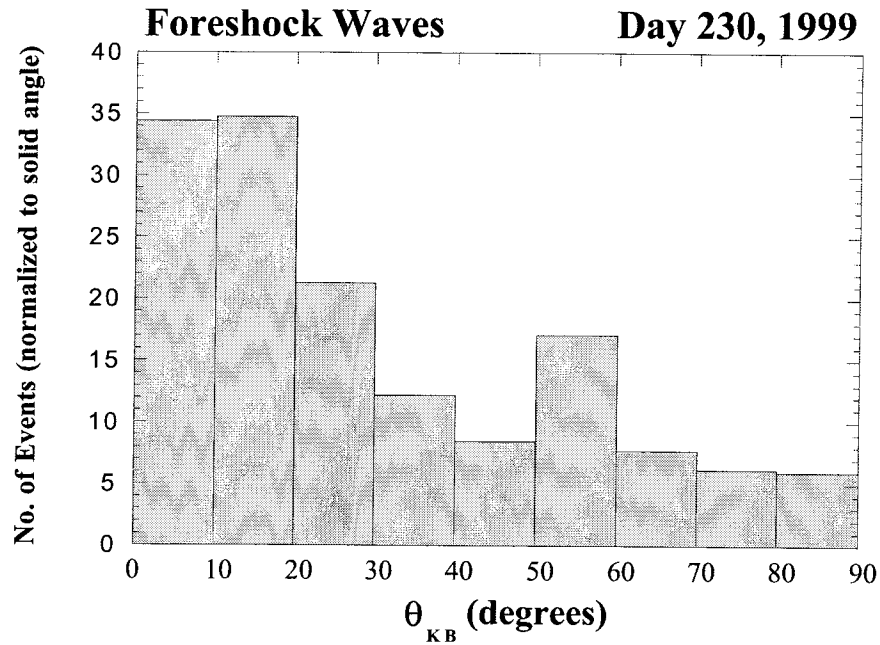


Fig. 11. A normalized histogram of the foreshock wave propagation directions.

of  $f \approx 1.25$  Hz waves. In another article focusing on the foreshock waves, Tsurutani et al. (2001) have demonstrated that small angular changes in the magnetic field orientation lead to orders of magnitude changes in wave power. These latter results were consistent with low-energy electron generation.

#### Magnetosheath Waves

A sample of the magnetosheath waves is shown in Figure 12. The waves have 5-6 s quasisinusoidal periods with peak-to-peak amplitudes of  $\sim 8$ -10 nT in a  $\sim 34$  nT field. The waves are thus highly nonlinear. There are large field magnitude decreases associated with some of the waves. The decreases involve field directional changes, thus they do not appear to be parts of mirror mode structures. It should be noted, however, that there is not a one-to-one association between waves and field decreases. There are more wave cycles than field decreases.

Figure 13 shows the wave-magnetic field decrease relationship in greater detail. Between the dashed vertical lines are 4 cycles of the waves. The magnetic field magnitude displays variations during two of the largest amplitude wave cycles (0157:07-0157:12 and 0157:12-0157:17 UT).

We will use two slightly different methods to determine the properties of the electromagnetic waves. We will use a minimum variance technique applied to single wave cycles and also applied to several wave cycles ("packets" - a packet is loosely defined as a number of cycles that appear to be roughly coherent) to compare and contrast the differences in the results. In some regions of space, wave properties vary from cycle-to-cycle, and thus multiple-cycle analyses could lead to a misunderstanding of the wave properties.

In Figure 14 we show the minimum variance analysis results for two consecutive wave cycles analyzed separately and also analyzed together (bottom panel). On the top is the cycle from 0157:03 - :08 UT and in the center, the cycle from 0157:08 - :15 UT. The wave cycle in the center is nearly circularly polarized in a left-hand sense, and is propagating at an angle of  $6^\circ$  relative to the ambient field. The wave is planar,  $\lambda_2/\lambda_3 = 14.2$ . The wave cycle in the center shows similar, but slightly different properties. The wave is planar ( $\lambda_2/\lambda_3 = 11.2$ ) and is polarized in the left-hand sense. The wave is propagating at  $18^\circ$  relative to the

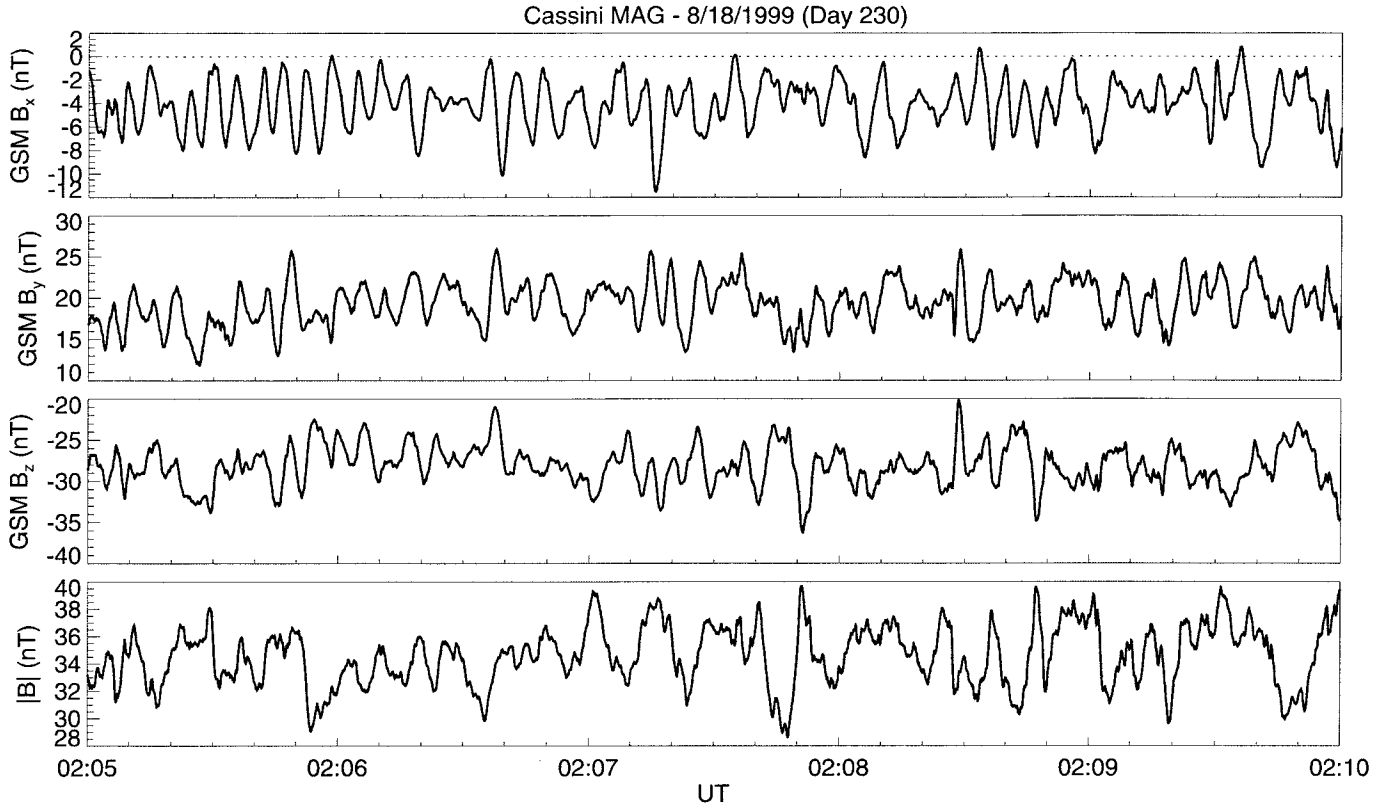


Fig. 12. Magnetosheath waves with 5 to 6 second quasiperiods and  $\sim 8$ -10 nT peak-to-peak amplitudes.

ambient magnetic field and is elliptically polarized ( $\lambda_1/\lambda_2 = 3.8$ ). The bottom panel shows the minimum variance results from the entire interval. Several differences can be noted: the multiple cycle “average” value indicates that the waves are far less planar ( $\lambda_2/\lambda_3 = 3.7$ ), they are more circularly polarized ( $\lambda_1/\lambda_2 = 1.8$ ), and the average propagation direction is nearly along  $\vec{B}_0$  ( $\theta_{kB} = 12.7^\circ$ ).

Wave “packets” and individual cycles throughout the magnetosheath passage have been analyzed. A summary of the results is given in Table 2. The third and fourth columns are the start and stop times of the wave interval analyzed, the fifth column the average period of the waves in the packets (“packets” are denoted by the roman numerals in the first column), and B is the average ambient field strength in units of nT. Almost all cycles examined were found to be left-hand polarized in the spacecraft frame (right-hand column).

There are several interesting wave features to note in this table. The waves vary from circular to elliptical polarizations and the angles of propagation relative to the ambient magnetic field vary from  $1^\circ$  to  $73^\circ$ . Most of the waves are propagating obliquely to the ambient magnetic field. There is a general tendency, although not a strong one, for the obliquely propagating waves to be more elliptically polarized. However, there are examples of circularly polarized waves found to be propagating at very large  $\theta_{kB}$  angles. An example can be found at 0205:48.6 to 05:55 UT ( $\lambda_1/\lambda_2 = 1.8$  and  $\theta_{kB} = 78^\circ$ ).

The properties of the entire “packets” are shown in gray tone. The level of polarization ( $\lambda_1/\lambda_2$ ) is typically near the minimum value of the individual cycle values within the packet. The angle of propagation  $\theta_{kB}$  is also near the minimum of values of the individual cycles. Individual wave cycles within a “packet” often have similar angles of propagation (but not always). On the other hand, the degree of polarization

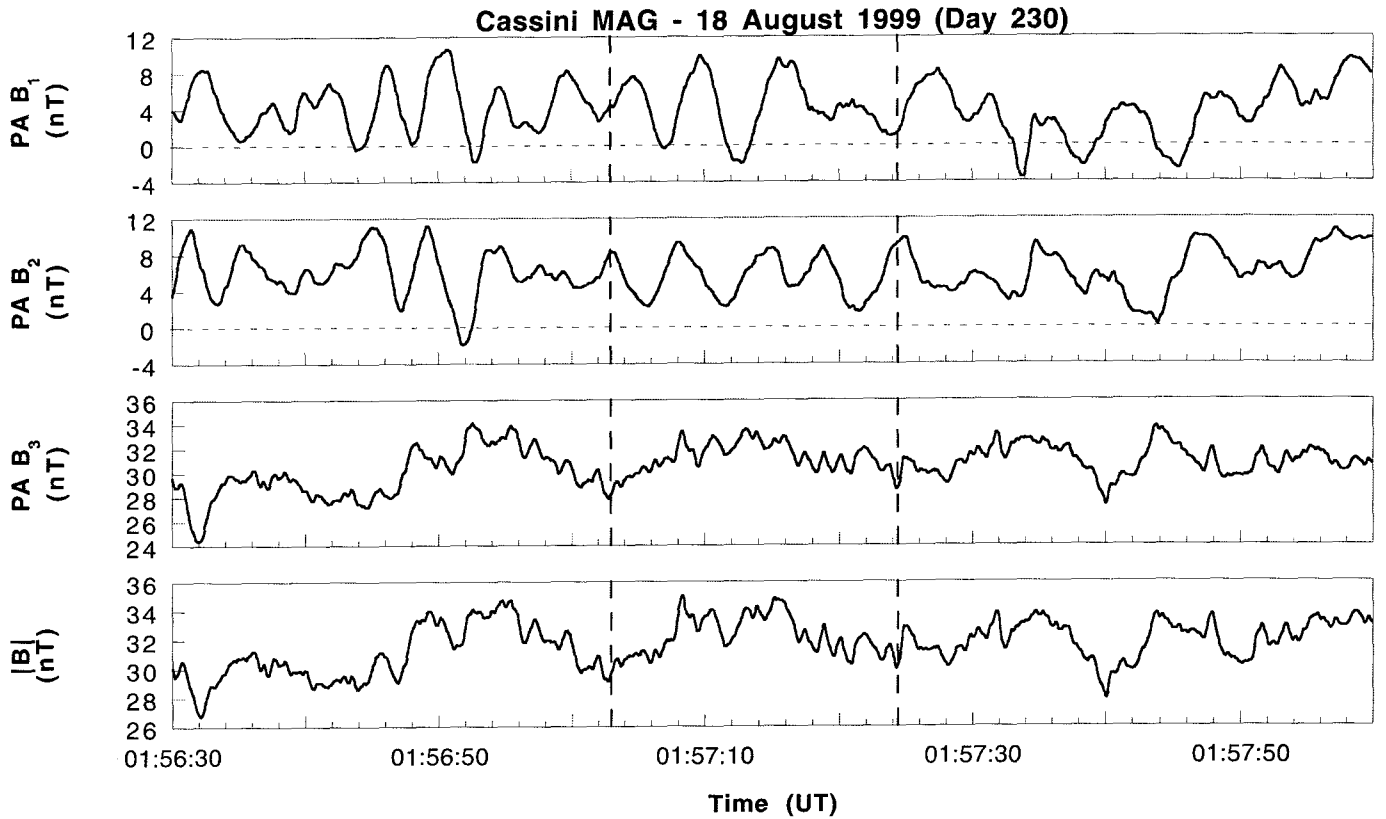


Fig. 13. Magnetosheath waves.

of cycles within a packet is typically highly mixed.

Figure 15 shows the magnetosheath wave frequency ( $f$ ) and the proton cyclotron frequency ( $f_p$ ) as a function of spacecraft location (and time). Magnetospheric waves are also included in this plot ( $T > 0232$  UT) but will not be discussed for the moment. The magnetosheath waves are noted to have frequencies of  $\sim 0.3$  to  $0.6 f_p$ .

Since the magnetosheath fields were essentially orthogonal to the Sun-earth line, the Doppler shift of the waves due to convection past the spacecraft was negligible. Thus the waves are left-hand polarized in the plasma frame and were propagating in the proton (ion) cyclotron mode. We believe that these are the largest amplitude proton cyclotron waves detected in geospace to date.

From an inspection of the magnetic field data, it was found that there was little or no indication of the presence of mirror mode structures. A search for field decreases with little or no changes in direction proved to be unfruitful. Few, if any, intense whistler lion roars (often associated with the high beta portions of mirror mode structures: Tsurutani et al., 1982; Zhang et al., 1998; Paschmann et al., 2000) were detected in the magnetosheath (G. Hospodarsky, personal communication, 2000).

#### Outer Magnetospheric Waves

An example of the outer magnetospheric waves is shown in Figure 16. The waves are quasi-sinusoidal with  $\sim 3$  s periods. The maximum peak-to-peak amplitudes are  $\sim 3.0$  nT in a  $\sim 61$  nT field (at  $\sim 0232:30$  UT). The wave amplitudes are largest in the transverse components (GSM  $B_y$  and  $B_x$ ). The ambient field is primarily in  $B_z$ , as expected for magnetospheric fields. The amplitude is largest in the  $B_y$  component and is considerably smaller in the  $B_x$  component. The waves sometimes have a compressional

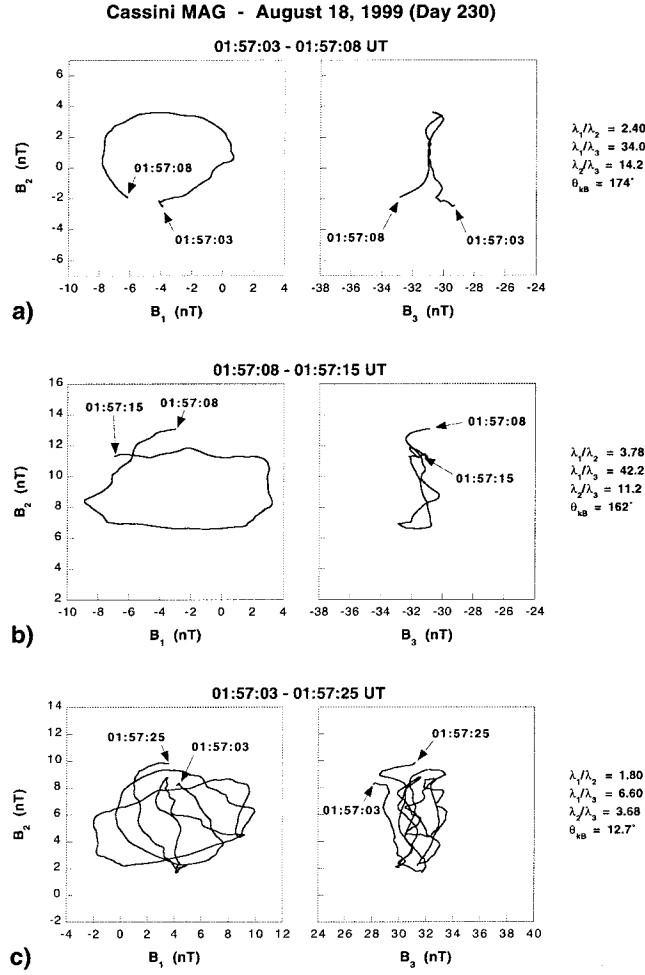


Fig. 14. Several magnetosheath wave cycles. The events were taken from the interval in Figure 12.

component. At  $\sim 0232:30$  UT, the magnetic magnitude (compressional) variations are on the order of  $\sim 0.5$  nT.

Figure 17 shows the waves in minimum variance coordinates and in higher time resolution. It is interesting to note that the amplitudes are largest (8.5 nT peak-to-peak) where the magnetic field increased from  $\sim 61$  to  $\sim 62$  nT. The interval between 0232:30 and 0232:46 UT has been used to determine the minimum variance coordinates for the whole interval of the figure. The  $B_3$  component oscillations are minimum in this region, indicating an accurate determination of the minimum variance direction. On the bottom (panel b) are the corresponding hodograms. The  $B_2 - B_1$  hodogram indicates that the waves are highly linearly polarized (consistent with the previous description of  $B_y$  and  $B_x$  amplitudes). The individual wave cycles are shifted from each other in the hodogram because of the spacecraft motion toward the Earth into higher magnetic field strengths (we specifically did not detrend the data). The  $B_2 - B_3$  hodogram shows that the waves are reasonably planar. The angle of propagation of the waves relative to the magnetic field was  $\sim 42^\circ$ .

Individual cycles of the magnetosheath waves have been analyzed and the results are given in Table 2. The range of polarization  $\lambda_1/\lambda_2$  is 1.4 to 27.5 and the range of angle  $\theta_{kB}$  was  $1^\circ$  to  $73^\circ$ .

Figure 18 shows another example of the outer magnetospheric waves, but later in time. The amplitudes are as large as  $\sim 2.0$  nT peak-to-peak in a  $\sim 69.0$  nT ambient field. There is a slight magnetic field

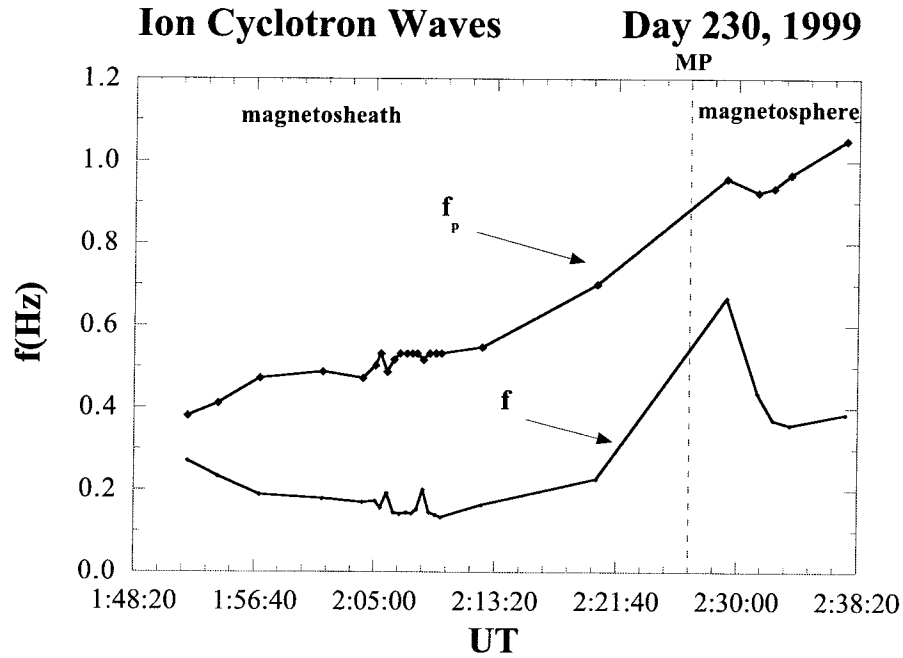


Fig. 15. Magnetosheath and magnetospheric wave frequency as a function of proton cyclotron frequency.

magnitude gradient where the waves were detected. The interval where the minimum variance analyses were performed is indicated by the two vertical dashed lines at 0237:24 UT and 0237:41 UT. Again there is very little variation along  $B_3$ , indicating a “good determination” of the minimum variance direction. The magnetic magnitude variations associated with the waves are quite small,  $\sim 0.2$  nT (note that the scale of the  $B_3$  component and  $|B|$  is much finer than for the other components).

The bottom panel (b) gives the hodogram results. These waves are left-hand elliptically polarized with  $\lambda_1/\lambda_2 = 2.9$ . The average angle of propagation is  $8.6^\circ$  relative to  $\vec{B}$ . The waves are highly plane polarized,  $\lambda_1/\lambda_3 = 212$  and  $\lambda_2/\lambda_3 = 73.1$ .

The magnetospheric wave results are itemized in Table 3. All of the waves analyzed were found to be left-hand circularly to linearly polarized ( $\lambda_1/\lambda_2$  up to 175) in the spacecraft frame. The  $\theta_{kB}$  values range from  $6^\circ$  to  $71^\circ$ . Some packets have nearly parallel propagating waves and other packets are off-axis propagating waves. Since there is little or no plasma convection to speak of, the waves must be left-hand polarized in the plasma frame. From Figure 15, the waves have a frequency  $f$  between  $0.3$  and  $0.5 f_p$ . The waves are therefore propagating in the proton cyclotron mode.

To determine the solar wind effects on the magnetosphere during this interval, we again examine the GEOTAIL ram pressure values/variations given in Figure 3. The interval of outer magnetospheric waves occurs from 0226 UT to 0238 UT (Figures 16 to 18). As previously stated, the time delay for the solar wind to travel from GEOTAIL to the magnetopause is  $\sim 4$  min. Thus, the relevant solar wind plasma parcel is from  $\sim 0222$  to 0234 UT.

Can one find solar wind features that lead to proton temperature anisotropies ( $T_\perp/T_\parallel > 1$ ) that cause ion cyclotron wave growth? There are no obvious large scale solar wind ram pressure fluctuations that caused the growth of the waves such as were found by Anderson and Hamilton (1993) in their events. However, the relationship between large amplitude waves and magnetic field increases noted in Figures 17 and 18 indicates that small ram pressure fluctuations may be present. If so, there could be small scale

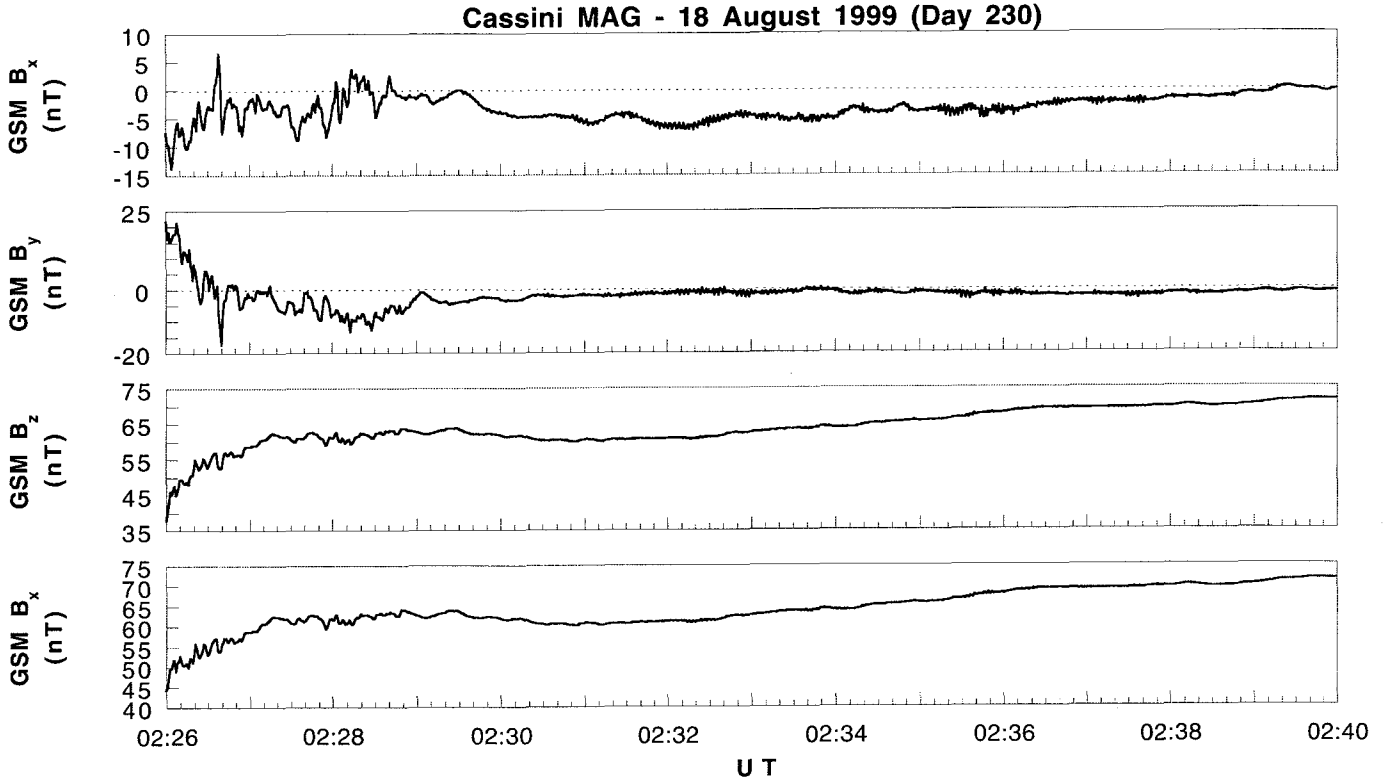


Fig. 16. Outer magnetospheric waves.

density enhancements that would easily be missed by GEOTAIL. Perhaps future Cluster II searches for small solar wind features and their effects will answer this question.

#### Particle Losses and Proton Auroras

The peak proton cyclotron wave amplitudes of  $\pm 1.7$  nT in a 61 nT field occurred at  $\sim 0232$  UT. The proton cyclotron frequency  $f_p$  was 0.93 Hz. The wave frequency  $f$  was  $\sim 0.35$  Hz. Assuming a wave phase velocity  $V_{ph} \approx 10^8 \text{ cm}^{-2} \text{ s}^{-1}$ , and using the first-order cyclotron resonance condition (1), one obtains a resonant proton parallel energy of  $\sim 10$  keV. The pitch angle diffusion rate is given by:

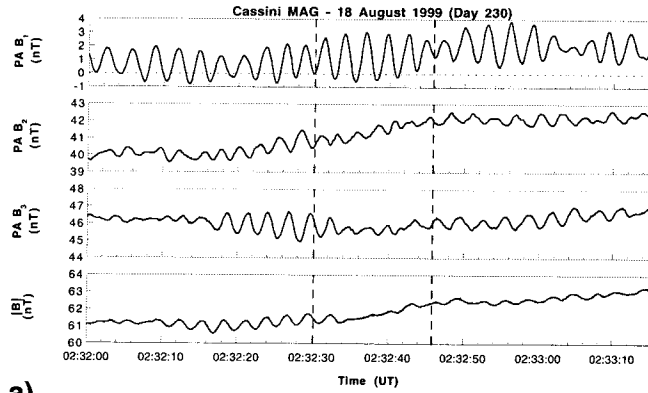
$$D_{\alpha\alpha} = 2\pi f_p \left( \frac{B_\omega}{B} \right)^2 \eta \quad (5)$$

from Kennel and Petschek (1966). With a value of  $B_\omega \approx 1.7$  nT, and assuming  $\eta$  the fractional amount of time the particle is in resonance with the wave is  $\approx 0.1$ ,  $D_{\alpha\alpha}$  is therefore  $\sim 7.2 \times 10^5 \text{ s}^{-1}$ , or  $T = 1.3 \times 10^4 \text{ s}$ . The bounce time  $T_b$  of a 10 keV proton is  $1.2 \times 10^2 \text{ s}$ . Thus the protons are on weak pitch angle diffusion. The resulting proton aurora due to wave-particle interactions would be expected to be weak and diffuse.

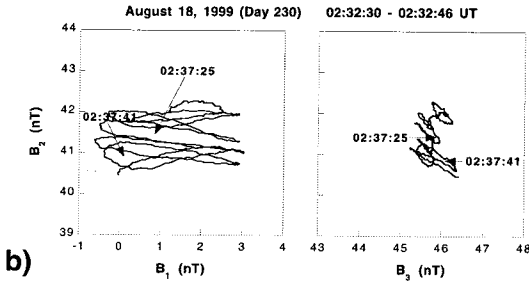
#### Magnetotail Waves

The Alfvénic  $B_s$  fluctuations (shown in Figure 6) caused magnetospheric substorms. Corresponding geomagnetic activity was high throughout the Cassini pass. This is shown in Figure 19. Substorms were occurring from  $\sim 0700$  to  $\sim 1200$  UT, the Cassini tail passage. Large amplitude waves in the tail lobe were detected primarily near two time regions,  $\sim 0820$  and  $1003$  UT. This is indicated in the figure.



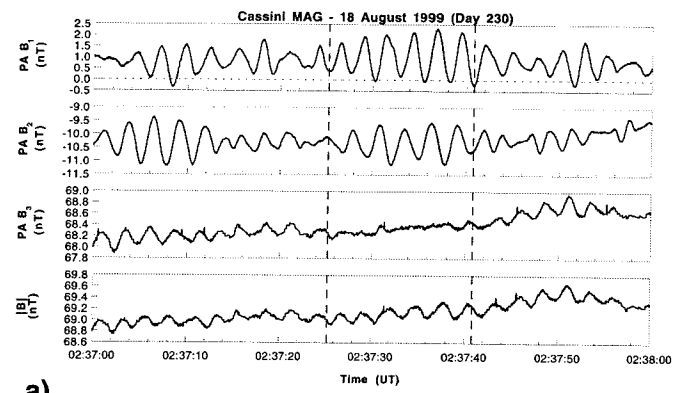


a)

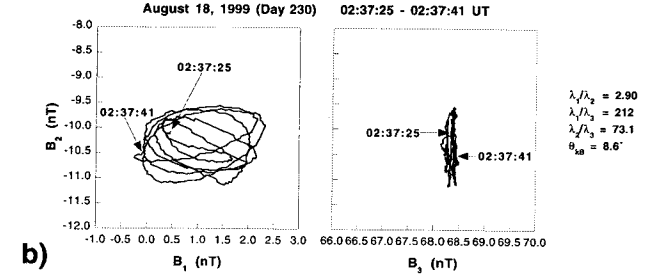


b)

Fig. 17. Hodogram of the 02:32:30 to 02:32:46 UT magnetospheric wave packet.



a)



b)

Fig. 18. A hodogram of the 02:37:24 to 02:37:41 UT wave packet.

One example of waves near the former interval is shown in Figure 20. The waves are transverse oscillations, and have  $\sim 7.5$  s periods. The peak-to-peak amplitudes are  $\sim 0.3$  nT in a  $\sim 16.1$  nT field. The compressional components are  $\leq 0.1$  nT. The three cycles from 0819:43.7 to 0820:07.6 UT are elliptically polarized ( $\lambda_1/\lambda_2 = 2.3$  to  $3.0$ ) and are propagating nearly along  $\vec{B}$  ( $6^\circ$  to  $26^\circ$ ).

Figure 20 shows an example of the waves detected in the second interval. Nearly purely compressional (longitudinal) oscillations with  $\sim 7.3$  s periods are present. The magnitudes are again small,  $\sim 0.1$  nT. The four cycles from 1003:15.6 to 1003:44.4 UT are compressive waves. The angles of propagation are highly oblique to  $\vec{B}$  ( $76^\circ$ ,  $84^\circ$ ,  $70^\circ$  and  $75^\circ$ ). We believe that this is the first time such purely compressional waves have been detected in the magnetotail.

The extremely thorough Cassini magnetic control program instituted by the Cassini Project has developed this very low-noise spacecraft (Mehlem and Narvaez, 1999). Without such a rigorous program it is probable that such new wave modes could not have been detected.

## SUMMARY

### Foreshock Waves

Foreshock whistler mode waves are detected in the region from the shock to  $\sim 1.8 R_e$  upstream. The waves have  $\sim 0.8$  s quasiperiods in the plasma frame and are right-hand circularly to elliptically polarized in the spacecraft frame. The angle of propagation to  $\vec{B}$  varies from  $6^\circ$  to  $88^\circ$ . The waves are compressive. It is argued that the waves are whistler mode emissions generated by electrons tens of eV in energy streaming towards the Sun. A more comprehensive analysis is presented in Tsurutani *et al.* (2001).

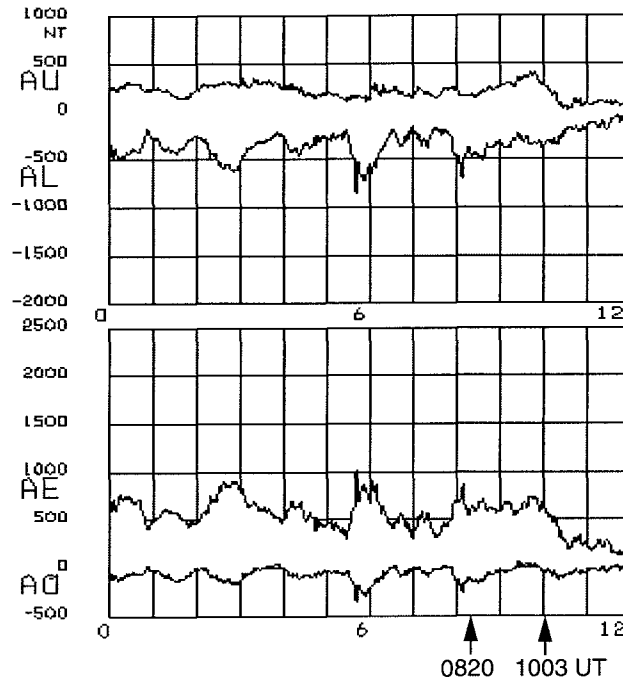


Fig. 19. Auroral zone geomagnetic indices during the Cassini flyby. Two intervals where LF waves were detected are indicated by arrows.

### Magnetosheath Waves

The magnetosheath waves are found to be left-hand circular to elliptically polarized with  $f = 0.3$  to  $0.6 f_p$ . They are generated by a temperature anisotropy instability with  $T_{\perp}/T_{\parallel} > 1$ . The anisotropy is created by the shock heating of solar wind protons, in direction perpendicular to the magnetic field. Behind the shock and throughout the sheath, the Zwan-Wolf (1976) draping effect will maintain a strong  $T_{\perp}/T_{\parallel} > 1$  anisotropy. The magnetosheath proton cyclotron waves are the most intense ion cyclotron waves detected in geospace to date.

### Magnetospheric Waves

The outer magnetosphere waves are also identified as proton cyclotron waves with frequencies between  $0.2$  to  $0.5 f_p$ . These waves are often highly elliptical to linearly polarized. The source of free energy is, however, somewhat of a mystery. At the time of wave occurrence, the large scale solar wind ram pressure was steady to decreasing. Small scale solar wind fluctuations cannot be ruled out, however.

### Magnetotail Waves

Two new modes were identified in the distant tail lobes, primarily due to the unusual sensitivity of the Cassini magnetometers and the spacecraft cleanliness program. A purely compressive ( $\sim 0.1$  nT) mode as well as a short period transverse wave mode were illustrated.

## CONCLUSIONS AND DISCUSSION

In the Cassini geospace wave survey, we find that much can be done to understand microinstabilities generating LF waves using magnetic field data alone. From our results, we have been able to make a variety of predictions of plasma and energetic particle pitch angle distributions (in the foreshock, magnetosheath and outer magnetosphere). In a follow-up effort, we will examine the plasma and

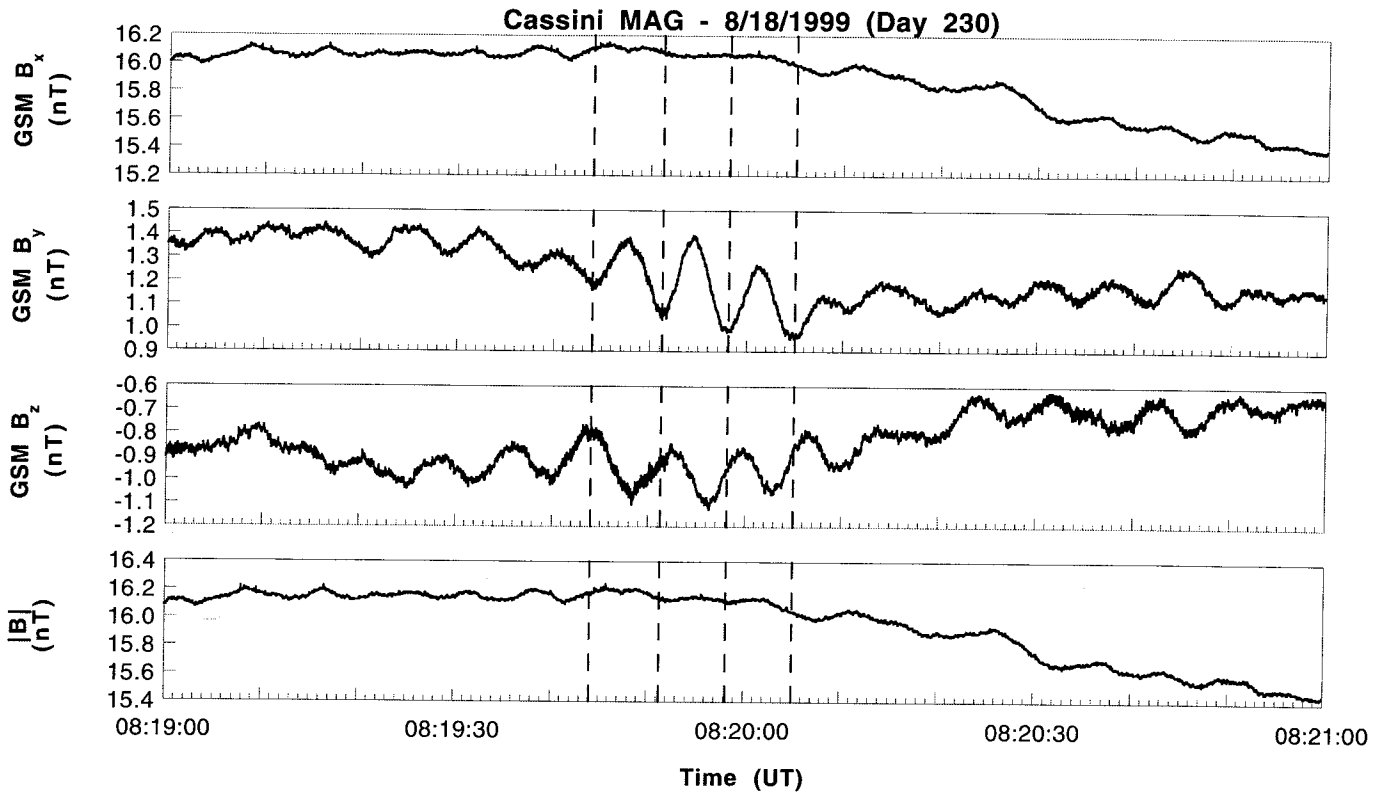


Fig. 20. Transverse  $\sim 7.5$  second oscillations in the magnetotail.

energetic particle and wave properties to determine if our conclusions/speculations in this paper were indeed correct or not.

This paper has shown that even though these four regions of space have been previously studied in very great detail, there is still much to learn and it is very worthwhile examining the waves in even greater detail. Cluster II will provide an opportunity for detailed studies of several of these regions.

Many surprises were found from this examination. In the upstream region, the standard picture is that ion beams stream from the shock/magnetosphere and populate this region. These beams generate foreshock waves. The waves and particles would be detected on field lines antisunward of the field tangent to the bow shock. This was shown in Figure 7. The mode typically reported in the literature (Hoppe, 1981; Smith et al., 1983; Tsurutani et al., 1993) has 10 - 60 s periods and is left-hand polarized in the spacecraft frame. These waves have been shown to be anomalously Doppler-shifted magnetosonic (right-hand) waves convected past the spacecraft.

Figure 7 shows a schematic of the electron and proton foreshocks for an interplanetary magnetic field angle of  $\sim 70^\circ$  relative to the Sun-Earth line. This is the correct geometry for the present case. Indicated on the right are the particle parallel kinetic energies needed to propagate upstream against a  $\sim 560 \text{ km s}^{-1}$  solar wind flow. It is clear that only very energetic protons can get upstream at all, while low energy electrons have easy access. Thus the "foreshock" is an almost purely electron foreshock. The access of shock accelerated/reflected electrons to the upstream region is controlled by the connection of the interplanetary magnetic field line to the bow shock (the IMF angle). Cases where the magnetic field angle connected and disconnected to the shock led to the presence of waves and then the disappearance of waves (not shown). One interesting new detail is the strong compressibility of the waves, presumably due to the large angles of  $\vec{k}$  relative to the ambient magnetic field (Figure 11). The strong off-axis character

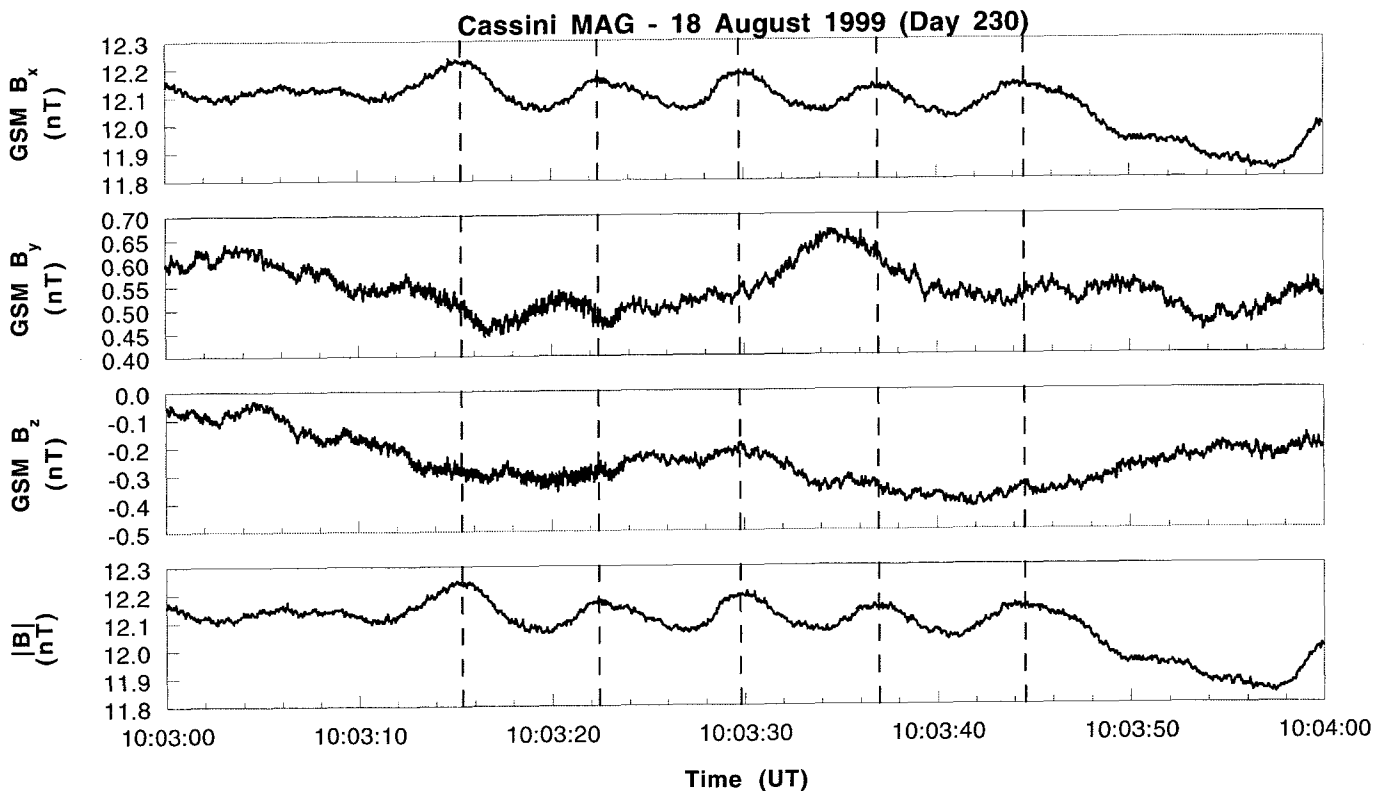


Fig. 21. Nearly purely compressional  $\sim 7.3$  s waves in the magnetotail.

has been explained by Sentman et al. (1983) and Wong and Smith (1994) as being due to a Landau interaction with the electrons. The full distribution of wave  $k$  values (Figure 11) may be related to the unusual electron distribution functions found in various parts of the foreshock (see Savoini and Lembege, 1994, 2001).

The magnetosheath waves are perhaps the biggest surprise. No mirror mode structures were detected. Only proton cyclotron waves were present and these had the largest amplitude (of ion cyclotron waves) detected in geospace to date. The ACE  $\text{He}^{++}/\text{H}^+$  density ratio was  $\sim 2.0\%$  for the solar wind plasma parcel that hit the bowshock at the time of the Cassini encounter. This low  $\text{He}^{++}$  density ratio (an average value of  $4.4\%$  has been found for high speed streams: McComas et al., 1996) is in qualitative agreement with the Price et al. (1986) and Gary et al. (1992) scenario of a reduction in size of the stop-band, thus an increase in the ion cyclotron growth rate. However, further modeling work needs to be done to understand if this is indeed the correct explanation or not. We further note that the  $\text{He}^{++}/\text{H}^+$  ratio varied from  $<1\%$  (at the peak of the event) to  $4\%$  (at the edges of the event) within the high-speed stream. Whether this variability is a feature of high-speed streams detected in the ecliptic plane where stream “edge effects” and fast stream-slow stream interactions are important, needs to be studied. Another possible explanation is that the presently used threshold for mirror instability is incorrect. Leubner and Schupfer (2001), examining non-thermal distributions, have indicated that the threshold can be significantly higher than previously thought. For these reasons, the variability of Jovian and Saturnian magnetosheath wave modes and intensities (also under the different plasma beta conditions) are of particular interest for future Cassini studies.

One possible scenario explaining the presence of dayside instabilities/waves is that the previously occurring substorms have led to proton injection in the midnight sector. With subsequent particle gradient and curvature drift to the dayside, the asymmetric shape of the magnetosphere (compressed

dayside) leads to particle drift-shell splitting (Roederer, 1967; Schulz, 1972), where particles with  $\sim 90^\circ$  pitch angle will drift to larger L than particles with near  $\sim 0^\circ$  pitch. This picture will lead to "patches" in the outer dayside magnetosphere where the proton cyclotron mode would be unstable. A second scenario, working in conjunction with the first, can lead to the enhanced wave growth. If sunlight heating of the ionosphere leads to upward flow of plasma and an enhanced magnetospheric cold population, the presence of this plasma would lead to a lowering of the resonant energy threshold for instability. A similar explanation has been proposed to explain enhanced chorus (electron temperature anisotropy instability) at local dawn (Jensch, 1976, Tsurutani and Smith, 1977) through the electron temperature anisotropy instability. A third factor discussed previously is the possible presence of small scale solar wind pressure pulses. At any rate, the proton cyclotron waves are clearly present and will lead to a steady "drizzle" of particles into the upper ionosphere. To determine the specific mechanisms, energetic particle pitch-angle information and plasma densities will have to be examined in detail. We hope to do this in the near future.

## ACKNOWLEDGMENTS

Portions of the research presented here were performed at the Jet Propulsion Laboratory, California Institute of Technology, Pasadena, under contract with the National Aeronautics and Space Administration.

## REFERENCES

- Anderson, B. T., and D. C. Hamilton, Electromagnetic Ion Cyclotron Waves Stimulated by Modest Magnetospheric Compressions, *J. Geophys. Res.*, **98**, 11369 (1993).
- Anderson, B. J., S. A. Fuselier, S. P. Gary, and R. E. Denton, Magnetic Spectral Signatures in the Earth's Magnetosheath and Plasma Depletion Layer, *J. Geophys. Res.*, **99**, 5877 (1994).
- Armstrong, T. P., M. E. Pesses, and R. B. Decker, Shock Drift Acceleration, in *Collisionless Shocks in the Heliosphere: Reviews of Current Research*, ed. B. T. Tsurutani and R. G. Stone, Geophys. Mon., **35**, pp. 271-285, Amer. Geophys. Union Press, Wash. D.C. (1985).
- Asbridge, J. R., S. J. Bame, and I. B. Strong, Outward Flow of Protons from the Earth's Bow Shock, *J. Geophys. Res.*, **73**, 5777 (1968).
- Baker, D. N., R. D. Belian, T. A. Fritz, P. R. Higbie, S. M. Krimigis, D. G. Sibeck, and R. D. Zwickl, Simultaneous Energetic Particle Observations at Geostationary Orbit and in the Upstream Solar Wind: Evidence for Leakage During the Magnetospheric Compression Event of November 1, 1984, *J. Geophys. Res.*, **93**, 14317 (1988).
- Bonifazi, C., and G. Moreno, Reflected and Diffuse Ions Backstreaming from the Earth's Bow Shock, 1. Basic Properties, *J. Geophys. Res.*, **86**, 4397 (1981a).
- Bonifazi, C., and G. Moreno, Reflected and Diffuse Ions Backstreaming from the Earth's Bow Shock, 2. Origin, *J. Geophys. Res.*, **86**, 4405 (1981b).
- Brinca, A. L., and B. T. Tsurutani, Influence of Multiple Ion Species on Low-Frequency Electromagnetic Wave Instabilities, *J. Geophys. Res.*, **94**, 13565 (1989).
- Chao, J. K., C. H. Lin, Y. H. Yang, X. Y. Wang, M. Kessel, C. H. Lin, S. H. Chen, and R. P. Lepping, Models for the size and shape of the Earth's magnetopause and bow shock, *J. Atmos. Sol. Terr. Phys.*, in press 2001.
- Cowley, S. W. H., R. J. Hynds, I. G. Richardson, P. W. Daly, T. R. Sanderson, K.-P. Wenzel, J. A. Slavin, and B. T. Tsurutani, Energetic Ion Regimes in the Deep Geomagnetic Tail: ISEE-3, *Geophys. Res. Lett.*, **11**, 275 (1984).
- Dougherty, M. K., S. Kellock, D. J. Southwood, A. Balogh, M. Barlow, T. Beek, M. W. Dunlop, R. White, E. J. Smith, L. Wigglesworth, M. Fong, R. Marquedant, B. T. Tsurutani, B. Gerlach, G. Musmann, K.-H. Glassmeier, H. Hartje, M. Rahm, I. Richter, C. T. Russell, D. Huddleston, R. C.

- Snare, G. Erdos, S. Szalai, F. M. Neubauer, S. W. H. Cowley, and G. L. Siscoe, The Cassini Magnetic Field Investigation, *Space Sci. Rev.*, submitted (2001).
- Dungey, J. W., Interplanetary Magnetic Field and the Auroral Zones, *Phys. Res. Lett.*, **6**, 47 (1961).
- Fairfield, D. H., Bow Shock Associated Waves Observed in the Far Upstream Interplanetary Medium, *J. Geophys. Res.*, **74**, 3541 (1969).
- Forman, M. A., and G. M. Webb, Acceleration of Energetic Particles, in *Collisionless Shocks in the Heliosphere: A Tutorial Review*, ed. R. G. Stone and B. T. Tsurutani, Geophys. Mon., **34**, pp. 91-114, Amer. Geophys. Union Press, Wash. D.C. (1985).
- Gary, S. P., C. D. Madland, and B. T. Tsurutani, Electromagnetic Ion Beam Instabilities, II., *Phys. Fluids*, **28**, 3691 (1985).
- Gary, S. P., Electromagnetic Ion/Ion Instabilities and their Consequences in Space Plasmas: A Review, *Space Sci. Rev.*, **56**, 373 (1991).
- Gary, S. P., The Mirror and Ion Cyclotron Anisotropy Instability, *J. Geophys. Res.*, **97**, 8519 (1992).
- Goldstein, M. L., H. K. Wong, A. F. Vinas, and C. W. Smith, Large Amplitude MHD Waves Up Stream of the Jovian Bow Shock: Reinterpretation, *J. Geophys. Res.*, **90**, 302 (1985).
- Goldstein, M. L., H. K. Wong, and A. Eviatar, Excitation of MHD Waves Upstream of Jupiter by Energetic Sulfur on Oxygen Ions, *J. Geophys. Res.*, **91**, 7954 (1986).
- Goodrich, C. C., Numerical Simulations of Quasi-Perpendicular Collisionless Shocks, in *Collisionless Shocks in the Heliosphere: Reviews of Current Research*, ed. B. T. Tsurutani and R. G. Stone, Geophys. Mon., **35**, pp. 153-168, Amer. Geophys. Union Press, Wash. D.C. (1985).
- Hoppe, M. M., C. T. Russell, L. A. Frank, T. E. Eastman, and E. W. Greenstadt, Upstream Hydromagnetic Waves and their Association with Backstreaming Ion Populations: ISEE 1 and 2 Observations, *J. Geophys. Res.*, **86**, 4471 (1981).
- Jensch, V., Electron Precipitation in the Morning Sector of the Auroral Zone, *J. Geophys. Res.*, **81**, 135 (1976).
- Kennel, C. F., and H. E. Petschek, Limit on stably trapped particle fluxes, *J. Geophys. Res.*, **71**, 1, 1966.
- Kennel, C. F., J. P. Edmiston, and T. Hada, A Quarter Century of Collisionless Shock Research, in *Collisionless Shocks in the Heliosphere: A Tutorial Review*, ed. R. G. Stone and B. T. Tsurutani, Geophys. Mon., **34**, pp. 1-36, Amer. Geophys. Union, Wash. D.C. (1985).
- Lee, M. A., Coupled Hydromagnetic Wave Excitation and Ion Acceleration Upstream of the Earth's Bow Shock, *J. Geophys. Res.*, **87**, 5063 (1982).
- Leubner, M.P., and N. Schupfer, A Universal Mirror Wave-mode Threshold Condition for Non-thermal Space Plasma Environments, *Eur. Geophys. Soc. Abstracts*, 215, 2001.
- McComas, D. J., G. W. Hoogeveen, J. T. Gosling, J. L. Phillips, M. Neugebauer, A. Balogh, and R. Forsyth, Ulysses Observations of Pressure-Balance Structures in the Polar Solar Wind, *Astron. Astrophys.*, **316**, 368 (1996).
- Mehlem, K., and P. Narvaez, Magnetostatic Cleanliness of Radioisotopic Thermoelectric Generators (RTGs) of Cassini, *IEEE*, 899 (1999).
- Papadopoulos, K., Microinstabilities and Anomalous Transport, in *Collisionless Shock in the Heliosphere: A Tutorial Review*, ed. R. G. Stone and B. T. Tsurutani, Geophys. Mon., **34**, pp. 59-90, Amer. Geophys. Union Press, Wash. D.C. (1985).
- Phillips, J. L., A. Balogh, S. J. Bame, B. E. Goldstein, J. T. Gosling, J. T. Hoeksema, D. J. McComas, M. Neugebauer, N. R. Sheeley, Jr., and Y. M. Wang, Ulysses at 50° South: Constant Immersion in the High-Speed Solar Wind, *Geophys. Res. Lett.*, **21**, 1105 (1994).
- Price, C. P., D. W. Swift, and L. C. Lee, Numerical Simulation of Nonoscillatory Mirror Waves at the Earth's Magnetosheath, *J. Geophys. Res.*, **91**, 101 (1986).
- Roederer, J. G., On the Adiabatic Motion of Energetic Particles in a Model Magnetosphere, *J. Geophys. Res.*, **72**, 981 (1967).
- Savoini, P., and B. Lembège, Electron Dynamics in Two- and One-dimensional Oblique Supercritical Collisionless Magnetosonic Shocks, *J. Geophys. Res.*, **99**, 6609, 1994.

- Savoini, P., and B. Lembége, Two-dimensional Simulations of a Curved Shock: Self-consistent Formation of the Electron Foreshock, to appear in *J. Geophys. Res.*, 2001.
- Schulz, M., Drift-Shell Splitting at Arbitrary Pitch Angle, *J. Geophys. Res.*, **77**, 624 (1972).
- Sentman, D. D., M. F. Thomsen, S. P. Gary, W. C. Feldman, and M. M. Hoppe, The oblique whistler instability in the Earth's foreshock, *J. Geophys. Res.*, **88**, 2048, 1983.
- Sibeck, D. G., R. W. McEntire, S. M. Krimigis, and D. N. Baker, The Magnetosphere as a Sufficient Source for Upstream Ions on November 1, 1984, *J. Geophys. Res.*, **93**, 14328 (1988).
- Smith, E. J., and B. T. Tsurutani, Magnetosheath Lion Roars, *J. Geophys. Res.*, **81**, 2261 (1976).
- Smith, E. J., B. T. Tsurutani, D. L. Chenette, T. F. Conlan, and J. A. Simpson, Jovian Electron Bursts, Correlation with the Interplanetary Field Direction and Hydromagnetic Waves, *J. Geophys. Res.*, **81**, 65 (1976).
- Smith, E. J., A. Balogh, M. Neugebauer, and D. McComas, Ulysses Observations of Alfvén Waves in the Southern and Northern Hemispheres, *Geophys. Res. Lett.*, **22**, 3381 (1995).
- Smith, C. W., M. L. Goldstein, and W. H. Mathaeus, Turbulence Analysis of the Jovian Upstream Wave Phenomena, *J. Geophys. Res.*, **88**, 5581 (1983).
- Sonnerup, B. U. O., and B. G. Ledley, Magnetopause Rotational Forms, *J. Geophys. Res.*, **79**, 4309 (1974).
- Thomsen, M. F., Upstream Suprathermal Ions, in *Collisionless Shocks in the Heliosphere: Reviews of Current Research*, ed. B. T. Tsurutani and R. G. Stone, *Geophys. Mon.*, **35**, pp. 253-270, Amer. Geophys. Union Press, Wash D.C. (1985).
- Tsurutani, B. T., and C. M. Ho, A Review of Discontinuities and Alfvén Waves in Interplanetary Space: Ulysses Results, *Rev. Geophys.*, **37**, 517 (1999).
- Tsurutani, B. T., and G. S. Lakhina, Some Basic Concepts of Wave-Particle Interactions in Collisionless Plasmas, *Rev. Geophys.*, **35**, 491 (1997).
- Tsurutani, B. T., and E. J. Smith, Two Types of Magnetospheric ELF Chorus and their Substorm Dependences, *J. Geophys. Res.*, **82**, 5112 (1977).
- Tsurutani, B. T., and E. J. Smith, Magnetosonic Waves Adjacent to the Plasma Sheet in the Distant Magnetotail: ISEE-3, *Geophys. Res. Lett.*, **11**, 331 (1984).
- Tsurutani, B. T., E. J. Smith, R. R. Anderson, K. W. Ogilvie, J. D. Scudder, D. N. Baker, and S. J. Bame, Lion Roars and Nonoscillatory Drift Mirror Waves in the Magnetosheath, *J. Geophys. Res.*, **87**, 6060 (1982).
- Tsurutani, B. T., I. G. Richardson, R. M. Thorne, W. Butler, E. J. Smith, S. W. H. Cowley, S. P. Gary, S.-I. Akasofu, and R. D. Zwickl, Observations of the Right-Hand Resonant Ion Beam Instability in the Distant Plasma Sheet Boundary Layer, *J. Geophys. Res.*, **90**, 12159 (1985).
- Tsurutani, B. T., D. J. Southwood, E. J. Smith, and A. Balogh, A Survey of Low Frequency Waves at Jupiter: The Ulysses Encounter, *J. Geophys. Res.*, **98**, 21203 (1993).
- Tsurutani, B. T., C. M. Ho, E. J. Smith, M. Neugebauer, B. E. Goldstein, J. S. Mok, J. K. Arballo, A. Balogh, D. J. Southwood, and W. C. Feldman, The Relationship Between Interplanetary Discontinuities and Alfvén Waves: Ulysses Observations, *Geophys. Res. Lett.*, **21**, 2267 (1994).
- Tsurutani, B. T., E. J. Smith, M. E. Burton, J. K. Arballo, C. Galvan, X.-Y. Zhou, D. J. Southwood, M. K. Dougherty, K.-H. Glassmeier, F. M. Neubauer, and J. K. Chao, Oblique "1-Hz" whistler mode waves in an electron foreshock: The Cassini near-Earth encounter, *J. Geophys. Res.*, in press 2001.
- Wong, H. K., and C. W. Smith, Electron beam excitation of upstream waves in the whistler mode frequency range, *J. Geophys. Res.*, **99**, 13,373, 1994.
- Zwan, B. J., and R. A. Wolf, Depletion of the Solar Wind Plasma Near a Planetary Boundary, *J. Geophys. Res.*, **81**, 1636 (1976).
- Zhang, Y., H. Matsumoto, and H. Kojima, Lion Roars in the Magnetosheath: GEOTAIL Observations, *J. Geophys. Res.*, **103**, 4615 (1998).

**Table 1.** Foreshock Waves. Day 230, 1999.

	Start Time	Stop Time	T	B	$\lambda_1/\lambda_2$	$\theta_{KB}$	Polarization
1	1:51:00.2	1:51:00.6	0.4	8	17.5	32	RH
2	1:51:00.7	1:51:00.9	0.2	8	1.9	69	RH
3	1:51:01.9	1:51:02.5	0.6	9	1.4	25	RH
4	1:51:02.5	1:51:03.7	1.2	9	1.3	44	RH
5	1:51:03.7	1:51:05.0	1.3	9	1.9	21	RH
6	1:51:05.0	1:51:05.6	0.6	9	3.7	35	RH
7	1:51:05.6	1:51:06.4	0.8	8	3.0	18	RH
8	1:51:06.7	1:51:07.3	0.6	8	1.7	60	LH
9	1:51:07.3	1:51:07.8	0.5	8	3.7	22	RH
10	1:51:07.8	1:51:08.2	0.4	8	7.3	11	RH
11	1:51:08.2	1:51:08.7	0.5	8	2.0	72	RH
12	1:51:08.8	1:51:09.3	0.5	9	4.3	28	RH
13	1:51:09.3	1:51:10.0	0.7	9	5.1	32	RH
14	1:51:10.2	1:51:10.7	0.5	8	5.0	79	LH
15	1:51:10.8	1:51:11.5	0.7	8	8.5	15	RH
16	1:51:11.6	1:51:12.0	0.4	8	3.0	47	RH
17	1:51:12.0	1:51:12.5	0.5	10	2.1	55	RH
18	1:51:12.5	1:51:13.2	0.7	9	3.3	39	RH
19	1:51:13.2	1:51:13.8	0.6	9	2.7	6	RH
20	1:51:13.8	1:51:14.6	0.8	8	3.5	86	RH
21	1:51:14.7	1:51:15.2	0.5	9	7.3	62	linear
22	1:51:15.3	1:51:16.5	1.2	10	4.6	46	RH
23	1:51:16.6	1:51:17.4	0.8	10	1.9	8	RH
24	1:51:17.5	1:51:18.7	1.2	8	2.9	15	RH
25	1:51:18.7	1:51:19.5	0.8	8	2.1	27	RH
26	1:51:19.5	1:51:20.3	0.8	8	3.1	17	RH
27	1:51:20.3	1:51:21.3	1.0	9	4.5	50	RH
28	1:51:21.2	1:51:21.9	0.7	10	2.6	25	RH
29	1:51:22.0	1:51:23.0	1.0	10	2.8	9	RH
30	1:51:23.0	1:51:23.5	0.5	8	4.4	67	RH
31	1:51:23.6	1:51:24.2	0.6	8	3.1	14	RH
32	1:51:24.2	1:51:25.1	0.9	9	3.0	18	RH
33	1:51:25.1	1:51:26.4	1.3	10	7.5	50	linear
34	1:51:26.5	1:51:27.4	0.9	8	2.7	37	RH
35	1:51:27.4	1:51:27.8	0.4	7	5.6	72	LH
36	1:51:27.9	1:51:28.8	0.9	8	1.4	85	LH
37	1:51:28.8	1:51:29.3	0.5	8	4.7	43	RH
38	1:51:29.2	1:51:30.5	1.3	15	10.3	55	RH
39	1:51:30.7	1:51:31.5	0.8	15	5.1	59	LH
40	1:51:31.5	1:51:32.3	0.8	15	2.7	50	RH
41	1:51:32.4	1:51:33.1	0.7	15	4.5	64	RH
42	1:51:33.1	1:51:33.8	0.7	15	7.4	59	linear
43	1:51:33.8	1:51:34.3	0.5	15	2.2	27	RH
44	1:51:34.3	1:51:34.9	0.6	15	2.1	64	RH
45	1:51:34.9	1:51:35.3	0.4	15	1.5	50	RH
46	1:51:35.3	1:51:36.1	0.8	15	8.2	51	RH
47	1:51:36.1	1:51:36.6	0.5	15	3.3	56	RH
48	1:51:36.8	1:51:37.1	0.3	15	7.8	44	RH
49	1:51:37.2	1:51:37.8	0.6	15	8.2	26	RH
50	1:51:37.9	1:51:38.6	0.7	15	1.3	59	RH
51	1:51:38.6	1:51:39.2	0.6	15	3.8	66	linear
52	1:51:39.5	1:51:39.8	0.3	15	2.4	20	RH
53	1:51:39.9	1:51:40.6	0.7	15	2.0	52	RH



54	1:51:40.7	1:51:41.4	0.7	15	1.8	38	RH
55	1:51:41.5	1:51:41.9	0.4	15	12.2	80	linear
56	1:51:41.9	1:51:42.5	0.6	15	3.3	88	RH
57	1:51:42.5	1:51:42.8	0.3	15	1.7	36	RH
58	1:51:42.8	1:51:43.2	0.4	15	1.6	77	RH
59	1:51:43.2	1:51:44.1	0.9	15	2.7	87	linear
60	1:51:44.1	1:51:44.8	0.7	25	8.4	76	RH
61	1:51:44.8	1:51:45.3	0.5	20	2.2	77	RH
62	1:51:45.4	1:51:45.9	0.5	20	2.7	52	LH
63	1:51:46.0	1:51:46.7	0.7	20	3.0	46	RH
64	1:51:46.8	1:51:47.1	0.3	30	4.3	53	RH
65	1:51:47.4	1:51:48.1	0.7	35	6.6	15	RH
66	1:51:48.2	1:51:48.6	0.4	35	8.2	19	RH
67	1:51:49.2	1:51:49.7	0.5	35	192.4	81	-

---

**Table 2.** Magnetosheath Waves. Day 230, 1999.

	Start Time	Stop Time	T	B	$\lambda_1/\lambda_2$	$\theta_{KB}$	Polarization
1	1:52:02.6	1:52:17.4	3.7	25	1.8	72	-
	1:52:02.6	1:52:06.6	-	-	16.9	71	linear
	1:52:06.6	1:52:09.8	-	-	3.4	73	-
	1:52:09.8	1:52:12.9	-	-	4.1	52	LH
	1:52:12.9	1:52:17.4	-	-	1.4	70	LH
2	1:54:07.8	1:54:20.7	4.3	27	1.9	32	LH
	1:54:07.8	1:54:12.2	-	-	11.6	56	LH
	1:54:12.2	1:54:16.1	-	-	1.5	31	LH
	1:54:16.2	1:54:20.7	-	-	5.1	50	LH
3	1:57:03.1	1:57:24.4	5.3	31	2.0	15	LH
	1:57:03.1	1:57:07.7	-	-	2.6	6	LH
	1:57:07.8	1:57:12.9	-	-	4.0	13	LH
	1:57:13.0	1:57:18.8	-	-	5.1	18	LH
	1:57:18.9	1:57:24.4	-	-	11.1	31	LH elliptical
4	2:01:22.9	2:01:45.4	5.6	32	3.2	24	LH
	2:01:22.9	2:01:28.7	-	-	4.5	3	LH
	2:01:28.7	2:01:34.4	-	-	4.0	49	LH
	2:01:34.4	2:01:39.3	-	-	10.8	79	LH
	2:01:39.4	2:01:45.4	-	-	3.0	16	LH
5	2:04:10.3	2:04:33.8	5.9	31	1.3	11	LH
	2:04:10.3	2:04:16.5	-	-	7.2	11	LH
	2:04:16.5	2:04:21.3	-	-	3.5	37	LH
	2:04:21.6	2:04:27.0	-	-	5.6	28	LH
	2:04:27.0	2:04:33.8	-	-	2.2	9	LH
6	2:05:06.2	2:05:29.2	5.8	33	2.8	32	-
	2:05:06.2	2:05:10.9	-	-	2.0	45	LH
	2:05:10.9	2:05:15.5	-	-	5.3	42	LH
	2:05:15.5	2:05:21.3	-	-	3.0	75	RH
	2:05:21.6	2:05:29.2	-	-	1.4	10	RH
7	2:05:29.4	2:05:55.0	6.4	35	2.1	6	LH
	2:05:29.4	2:05:36.1	-	-	1.7	28	LH
	2:05:36.1	2:05:41.9	-	-	2.1	56	LH
	2:05:41.9	2:05:48.6	-	-	4.9	12	LH
	2:05:48.6	2:05:55.0	-	-	1.8	78	LH
8	2:05:55.0	2:06:21.2	5.2	32	1.9	15	LH
	2:05:55.0	2:06:00.0	-	-	3.5	14	LH
	2:06:00.0	2:06:06.3	-	-	2.4	20	LH
	2:06:06.3	2:06:11.1	-	-	8.5	32	LH
	2:06:11.1	2:06:16.4	-	-	9.9	81	linear
9	2:06:16.4	2:06:21.2	-	-	2.0	31	LH
	2:06:21.2	2:06:48.7	6.9	34	1.8	12	LH
	2:06:21.2	2:06:27.8	-	-	2.3	84	LH
	2:06:35.4	2:06:42.5	-	-	1.7	19	LH
	2:06:42.5	2:06:48.7	-	-	1.6	9	LH
10	2:06:48.7	2:07:17.0	7.1	35	1.2	30	LH
	2:06:48.7	2:06:56.6	-	-	2.3	24	linear
	2:06:56.6	2:07:04.4	-	-	2.4	50	LH
	2:07:04.4	2:07:11.6	-	-	1.4	11	LH/linear
	2:07:11.6	2:07:17.0	-	-	1.8	13	LH
11	2:07:17.0	2:07:37.6	6.9	35	3.3	15	LH
	2:07:17.0	2:07:22.8	-	-	4.1	63	LH
	2:07:22.8	2:07:29.8	-	-	3.8	80	LH
	2:07:29.8	2:07:37.6	-	-	1.3	7	LH

12	2:07:37.6	2:07:58.5	7.0	35	2.7	90	-
	2:07:37.6	2:07:44.2	-	-	2.0	50	LH
	2:07:44.2	2:07:50.7	-	-	2.1	77	linear
	2:07:50.7	2:07:58.5	-	-	6.2	69	linear
13	2:07:58.5	2:08:24.7	6.6	35	1.1	26	LH
	2:07:58.5	2:08:03.7	-	-	7.0	48	LH
	2:08:03.7	2:08:10.2	-	-	1.9	9	linear
	2:08:10.2	2:08:18.0	-	-	2.2	34	LH
14	2:08:18.0	2:08:24.7	-	-	2.7	79	LH
	2:08:24.7	2:08:49.7	5.0	34	2.3	52	LH
	2:08:24.7	2:08:28.9	-	-	5.2	69	LH
	2:08:28.9	2:08:33.1	-	-	4.7	27	LH
15	2:08:33.1	2:08:39.8	-	-	1.7	44	LH
	2:08:39.8	2:08:44.1	-	-	4.9	60	linear
	2:08:44.2	2:08:49.7	-	-	11.5	43	LH/elliptical
	2:08:49.7	2:09:17.5	6.9	35	1.7	52	-
16	2:08:49.7	2:08:53.6	-	-	2.6	60	linear
	2:08:53.6	2:09:05.3	-	-	1.3	64	LH
	2:09:05.6	2:09:11.8	-	-	4.5	61	LH
	2:09:11.8	2:09:17.5	-	-	3.4	78	RH
17	2:09:17.5	2:09:39.0	7.2	35	2.1	63	-
	2:09:17.5	2:09:24.7	-	-	3.1	65	RH
	2:09:25.3	2:09:30.0	-	-	2.9	31	LH
	2:09:30.0	2:09:39.0	-	-	3.9	32	LH
18	2:09:39.0	2:10:01.5	7.5	35	2.7	50	LH
	2:09:39.0	2:09:47.6	-	-	2.9	42	-
	2:09:47.6	2:09:56.5	-	-	3.8	81	LH
	2:09:56.5	2:10:01.5	-	-	1.4	40	LH
19	2:12:27.1	2:12:45.5	6.1	36	2.7	11	LH
	2:12:27.1	2:12:32.7	-	-	8.9	35	LH
	2:12:32.7	2:12:37.9	-	-	6.1	66	RH
	2:12:37.9	2:12:45.5	-	-	1.6	35	LH
19	2:20:18.3	2:20:31.5	4.4	46	5.0	2	LH
	2:20:18.3	2:20:22.2	-	-	1.8	14	LH
	2:20:22.2	2:20:25.7	-	-	2.7	9	LH
	2:20:25.7	2:20:31.5	-	-	33.0	1	LH

**Table 3.** Magnetospheric Waves. Day 230, 1999.

	<b>Start Time</b>	<b>Stop Time</b>	<b>T</b>	<b> B </b>	$\lambda_1/\lambda_2$	$\theta_{KB}$	<b>Polarization</b>
<b>1</b>	2:29:15.2	2:29:18.3	1.5	63	1.9	29	LH
	2:29:15.2	2:29:16.7	-	-	3.4	32	LH
	2:29:16.7	2:29:18.3	-	-	1.6	26	LH
<b>2</b>	2:31:27.1	2:31:33.9	2.3	60.7	4.0	7	LH
	2:31:27.1	2:31:29.3	-	-	1.5	13	LH
	2:31:29.3	2:31:31.6	-	-	27.1	18	LH
	2:31:31.6	2:31:33.9	-	-	8.3	7	LH
<b>3</b>	2:32:29.9	2:32:46.1	2.7	61.4	5.5	41	linear
	2:32:29.9	2:32:32.7	-	-	20.2	23	LH elliptical
	2:32:32.7	2:32:35.4	-	-	42.9	17	LH elliptical
	2:32:35.5	2:32:38.1	-	-	174.8	62	linear
	2:32:38.2	2:32:41.1	-	-	106.4	37	linear
	2:32:41.1	2:32:43.6	-	-	24.7	71	LH elliptical
	2:32:43.6	2:32:46.1	-	-	21.4	20	linear
	2:33:40.0	2:33:51.1	2.8	63.6	1.6	21	LH
<b>4</b>	2:33:40.0	2:33:42.7	-	-	5.2	18	LH
	2:33:42.8	2:33:45.2	-	-	2.7	31	LH
	2:33:45.3	2:33:48.0	-	-	2.5	23	LH
	2:33:48.1	2:33:51.1	-	-	2.4	23	LH
	2:37:30.5	2:37:43.4	2.6	69.1	2.9	9	LH
<b>5</b>	2:37:30.5	2:37:33.3	-	-	2.5	6	LH
	2:37:33.5	2:37:35.8	-	-	4.0	10	LH
	2:37:35.8	2:37:38.1	-	-	2.8	10	LH
	2:37:38.1	2:37:40.8	-	-	9.5	13	LH
	2:37:40.8	2:37:43.4	-	-	10.0	17	linear